

AperTO - Archivio Istituzionale Open Access dell'Università di Torino

**A possible new UHP unit in the Western Alps as revealed by ancient Roman quern-stones from Costigliole Saluzzo, Italy**

**This is a pre print version of the following article:**

*Original Citation:*

*Availability:*

This version is available <http://hdl.handle.net/2318/1565906> since 2019-04-08T16:13:22Z

*Published version:*

DOI:10.1127/ejm/2016/0028-2531

*Terms of use:*

Open Access

Anyone can freely access the full text of works made available as "Open Access". Works made available under a Creative Commons license can be used according to the terms and conditions of said license. Use of all other works requires consent of the right holder (author or publisher) if not exempted from copyright protection by the applicable law.

(Article begins on next page)

1 **Cover page**

2

3 **Title:** A new UHP unit in the Western Alps possibly revealed by ancient Roman quern-stones from  
4 Costigliole Saluzzo, Italy

5

6 **Running title:** Ancient quern-stones might reveal a new UHP unit in the Alps

7

8

9 **Detailed plan of the article (i.e. hierarchy of headings and subheadings)**

10 1. Introduction

11 2. Methods

12 2.1 Micro-X-ray fluorescence ( $\mu$ -XRF) maps

13 2.2 Micro-Raman spectroscopy

14 2.3 Mineral chemistry

15 2.4 YAG (Y-in-garnet) thermometry

16 2.5 Phase diagrams computation

17 3. Petrography and mineral chemistry

18 4. Phase equilibria and P-T evolution

19 4.1 Stability field of the chloritoid + glaucophane + garnet  $\pm$  talc assemblage: previous studies

20 4.2 Thermodynamic modelling of the chloritoid + glaucophane + garnet + talc stability field

21 4.3 P-T evolution

22 5. Discussion

23 5.1 Petrogenesis of the coesite-bearing chloritoid + garnet  $\pm$  glaucophane talcschists

24 5.1.1 *Mg-rich protoliths metamorphosed in a closed-system*

25 5.1.2 *Felsic or mafic protoliths metamorphosed in an open-system (i.e. metasomatic*  
26 *protoliths)*

27 5.2 Possible evidence for a new UHP unit in the southern Dora-Maira Massif

28 References

29 Figure captions

30

31

32 **Corresponding author:**

33 Simona Ferrando

34 [simona.ferrando@unito.it](mailto:simona.ferrando@unito.it)

35 Tel. +39/0116705106

36 Fax: +39/0116705128

37 **Title page**

38

39 **A new UHP unit in the Western Alps possibly revealed by ancient Roman quern-stones**  
40 **from Costigliole Saluzzo, Italy**

41

42

43

44 Chiara Groppo<sup>1,2</sup>, Simona Ferrando<sup>1\*</sup>, Daniele Castelli<sup>1</sup>, Diego Elia<sup>3</sup>, Valeria Meirano<sup>3</sup>, Luca  
45 Facchinetti<sup>3</sup>

46

47

48

49 <sup>1</sup>Department of Earth Sciences, Via Valperga Caluso 35, I-10128 Torino, Italy

50 <sup>2</sup>IGG-CNR, Via Valperga Caluso 35, I-10128 Torino, Italy

51 <sup>3</sup>Department of Historical Studies, Via S. Ottavio 20, I-10124 Torino, Italy

52 \*simona.ferrando@unito.it

53

54 **Abstract**

55 Peculiar coesite + chloritoid + garnet ± glaucophane talcschists have been used to make at least six  
56 quern-stones, unearthed in the ruins of a *villa rustica* belonging to the Roman imperial period and  
57 located at Costigliole Saluzzo, Western Alps. The site of the *villa rustica* and the presence of coesite  
58 relics suggest a possible provenience of these rocks from the ultra-high pressure (UHP) Brossasco-  
59 Isasca Unit (BIU) of the southern Dora-Maira Massif. However, similar talcschists have never been  
60 reported from this Unit.

61 Two samples of coesite-bearing, chloritoid + garnet ± glaucophane –talcschist collected from  
62 two different specimens of quern-stones, have been petrologically investigated with the aim of  
63 constraining their peak P-T conditions. The stability field of the coesite + garnet + talc + chloritoid +  
64 glaucophane assemblage has been constrained using isochemical phase diagrams modelled in the  
65 MnNCFMASHO system; prograde P-T conditions have been additionally constrained using the  
66 yttrium-in-garnet (YAG) geothermometer. Thermodynamic modelling tightly constrains peak P-T  
67 conditions at 480-510°C, 27-31 kbar.

68 The unusual Mg-rich composition of the talcschists suggest that they originated by Mg-  
69 metasomatism of either a granodioritic protolith or a Fe-rich metapelitic protolith. A mechanism  
70 similar to that constrained for the well-known pyrope-bearing whiteschists of the UHP BIU, i.e. influx  
71 of antigorite-derived fluids along shear zones during subduction, can be therefore envisaged.

72 Although the field occurrence of these coesite + chloritoid + garnet ± glaucophane talcschists  
73 is still unknown, the obtained results clearly show that these rocks cannot belong to the UHP BIU,  
74 whose peak P-T conditions are at significantly higher T and P (730°C, 40-43 kbar). Therefore, this  
75 finding opens the challenging hypothesis of the existence of a further, still unmapped, UHP Unit in  
76 the Southern Dora-Maira Massif that also experienced UHP metamorphism and fluid influx from  
77 underlying serpentinites during subduction. A detailed mapping and petrologic investigation of the  
78 tectono-metamorphic units adjacent to the BIU is required, in order to further constrain the location  
79 and the dimension of this new UHP unit in the framework of the southern Dora-Maira Massif.

80  
81 **Key-words:** coesite + chloritoid + garnet + glaucophane talcschist; UHP metamorphism; Mg-  
82 metasomatism; southern Dora-Maira Massif; thermodynamic modeling; micro-Raman spectroscopy

## 83 1. Introduction

84 The ruins of a wide *villa rustica* belonging to the Roman imperial period were unearthed at the  
85 southern periphery of the modern village of Costigliole Saluzzo (Fig. 1) and are still under excavation  
86 (Elia & Meirano 2012; Elia *et al.*, 2013). In its major phase, the main building reached an extent of  
87 around 5000 square metres. The evidence recovered supports the identification of two different  
88 sections in the *villa*, the *pars urbana*, with a residential function, and the *pars rustica*, destined to  
89 stocking agricultural products and to housing the productive units. Many fragments of quern-stones,  
90 pertaining to at least 6 specimens, were retrieved in the building, mainly from a wide room which  
91 acted as a kitchen and a butlery as well (Fig. 1b). The majority of the artefacts were in use when the  
92 villa was destroyed by a fire at the end of the III c. AD. The hand-mills, up to 34-39 cm in diameter  
93 (Fig. 2a,b), belong to two different types: a simpler and more common one, and a second type  
94 provided with a particular mechanism in order to obtain different qualities of refined cereals (Fig. 2c).  
95 They were carved from at least two different lithologies: (i) a coesite-bearing (micro-Raman  
96 identification), chloritoid + garnet ± glaucophane –talcschist (Fig. 2d-f), and (ii) a phengite + garnet +  
97 chloritoid ± glaucophane schist, with glaucophane pseudomorphically replaced by fine-grained  
98 aggregates of white mica + biotite + albite.

99 The location of the ancient quarry is still unknown. Costigliole Saluzzo is located at the mouth  
100 of Varaita Valley, some 5 km east of the ultra-high pressure (UHP) Brossasco-Isasca Unit (BIU),  
101 tectonically sandwiched between the high-pressure (HP) San Chiaffredo and Rocca Solei Units of the  
102 southern Dora-Maira Massif (Compagnoni *et al.*, 2012; Castelli *et al.*, 2014, with refs.) (Fig. 1a). The  
103 site of the *villa rustica*, then, clearly points to a provenience of these rocks from the southern Dora-  
104 Maira Massif. The presence of coesite relics seems to constrain the area of provenience to the UHP  
105 BIU. However, talcschists with a similar mineral assemblage have never been reported from this Unit.  
106 Therefore, this finding opens two challenging hypotheses: (i) the occurrence of still unrecognized,  
107 peculiar “whiteschist” within the BIU; (ii) the existence of a second, still unmapped, UHP unit in the  
108 southern Dora-Maira Massif.

109 In order to solve this conundrum, two samples of coesite-bearing, chloritoid + garnet ±  
110 glaucophane –talcschist collected from two different specimens of quern-stones, have been  
111 petrologically investigated with the aim of constraining their peak P-T conditions. The stability field of  
112 the coesite + garnet + talc + chloritoid + glaucophane assemblage has been constrained using  
113 isochemical phase diagrams modelled in the MnNCFMASHO system. Prograde P-T conditions have  
114 been additionally constrained using the yttrium-in-garnet (YAG) geothermometer. The genesis of  
115 these talcschists is discussed, considering two different possibilities: (i) derivation from a Mg-rich  
116 protolith metamorphosed in a closed system, or (ii) metasomatic product of a mafic or felsic (either  
117 granodiorite or metapelite) protolith.

118 The obtained results clearly suggest the existence of an UHP unit, whose peak P-T conditions  
119 lies inside the coesite stability field but at significantly lower temperature than those estimated for  
120 the BIU. A detailed mapping and petrologic investigation of the tectono-metamorphic units adjacent  
121 to the BIU is required, in order to further constrain the location and the dimension of this new UHP  
122 unit in the framework of the southern Dora-Maira Massif.

123

## 124 2. Methods

### 125 2.1 Micro-X-ray fluorescence (μ-XRF) maps

126 The micro-XRF maps of the whole thin sections (Fig. 3) were acquired using a μ-XRF Eagle III-XPL  
127 spectrometer equipped with an EDS Si(Li) detector and with an Edax Vision32 microanalytical system

128 (Department of Earth Sciences, University of Torino, Italy). The operating conditions were as follows:  
129 100 ms counting time, 40 kV accelerating voltage and a probe current of 900  $\mu\text{A}$ . A spatial resolution  
130 of about 65  $\mu\text{m}$  in both x and y directions was used. Quantitative modal percentages of each mineral  
131 were obtained by processing the  $\mu\text{-XRF}$  maps with the software program "Petromod" (Cossio *et al.*  
132 2002).

133

## 134 **2.2 Micro-Raman spectroscopy**

135 Micro-Raman spectra and map were acquired using the integrated micro/macro-Raman LABRAM  
136 HRVIS (Horiba Jobin Yvon Instruments) of the Interdepartmental Center "G. Scansetti" (Department  
137 of Earth Sciences, University of Torino, Italy), equipped with a computer-controlled, automated X-Y  
138 mapping stage. Excitation lines at 532 nm (solid-state Nd laser and 80 mW of emission power) were  
139 used, with Edge filter and a grating of 600 grooves/mm. Calibration was performed using the 520.6  
140  $\text{cm}^{-1}$  Si band. Each spectrum was collected by three accumulations of 5 s and with a laser spot of 4  
141  $\mu\text{m}$ . The map of 140  $\mu\text{m}$  x 45  $\mu\text{m}$ , with steps of 1  $\mu\text{m}$  and a laser spot of 4  $\mu\text{m}$ , was acquired on the  
142 sample surface by one accumulations of 1 s each step.

143

## 144 **2.3 Mineral chemistry**

145 Minerals were analysed with a Cambridge Stereoscan 360 SEM equipped with an EDS Energy 200 and  
146 a Pentafet detector (Oxford Instruments) at the Department of Earth Sciences, University of Torino.  
147 The operating conditions were as follows: 50 s counting time and 15 kV accelerating voltage. SEM-  
148 EDS quantitative data (spot size = 2  $\mu\text{m}$ ) were acquired and processed using the Microanalysis Suite  
149 Issue 12, INCA Suite version 4.01; natural mineral standards were used to calibrate the raw data; the  
150  $\rho\phi Z$  correction (Pouchou & Pichoir, 1988) was applied. Absolute error is 1  $\sigma$  for all calculated oxides.

151 A JEOL 8200 Superprobe (WDS) was used at the Department of Earth Sciences, University of  
152 Milano (Italy). Acceleration voltage was set to 15 kV, beam current was 15 nA and natural minerals  
153 were used as standards. A  $\rho\phi Z$  routine was used for matrix correction.

154 Mineral chemical data of representative minerals are reported in Fig.5, 6 and in Tables 1-2.

155

## 156 **2.4 YAG (yttrium-in-garnet) thermometry**

157 Temperature conditions for the growth of garnet core have been constrained by applying the  
158 yttrium-in-garnet thermometry (YAG) of Pyle & Spear (2000). This empirical geothermometer  
159 correlates the yttrium content in garnet with its temperature of formation, and is particularly  
160 suitable for xenotime-bearing metapelites that experienced metamorphic temperature in the range  
161 450-550  $^{\circ}\text{C}$ ; errors estimated in this temperature interval are, in fact, of few degrees.

162

## 163 **2.5 Phase diagrams computation**

164 Isochemical phase diagrams were calculated in the MnNCFMASHO system using Perple\_X (version  
165 6.7.2, Connolly 1990, 2009) and the thermodynamic dataset and equation of state for  $\text{H}_2\text{O}-\text{CO}_2$  fluid  
166 of Holland & Powell (2011). The following solid solution models were used: garnet (White *et al.*,  
167 2005), talc (ideal), chloritoid (Smye *et al.*, 2000), carpholite (Smye *et al.*, 2000), staurolite (ideal),  
168 chlorite (Holland *et al.*, 1998), Na-amphibole (Dale *et al.*, 2000), plagioclase (Newton *et al.*, 1980),  
169 omphacite (Diener & Powell, 2011) and epidote (Holland & Powell, 1998). Kyanite, quartz/coesite,  
170 lawsonite, paragonite, magnetite and hematite were considered as pure end-members.

171 The bulk rock compositions of the studied samples have been calculated by combining the  
172 mineral proportions obtained from the modal estimate of micro-XRF maps (Fig. 3) with mineral

173 chemistry acquired at SEM–EDS and WDS, and are reported in Table 3: these whole rock  
174 compositions have been used to model the growth of garnet core, in equilibrium with chloritoid and  
175 glaucophane cores. The possible effects of chemical fractionation of the bulk composition due to the  
176 growth of the strongly zoned garnet porphyroblasts have been also considered. The bulk  
177 compositions effectively in equilibrium during the growth of garnet rim have been therefore  
178 calculated by subtracting the garnet core and mantle compositions to the whole rock compositions  
179 (Table 3).

180

### 181 **3. Petrography, mineral chemistry and Raman spectroscopy**

182 The coesite-bearing chloritoid + garnet + glaucophane -talcschists (samples US900 and US773)  
183 consist of quartz/coesite, talc, garnet, chloritoid, glaucophane, late Mg-chlorite (Fig.3, 4), abundant  
184 accessory rutile, apatite and pyrite and minor xenotime (both in the matrix and in garnet). Mineral  
185 assemblages and compositions are similar in both the samples, but mineral modes are quite  
186 different. Sample US900 is quartz/coesite-, talc- and glaucophane -richer (vol%: Qz 38, Tlc 30, Cld 14,  
187 Gln 9, Grt 8; mineral abbreviation after Whitney & Evans, 2010) than sample US773. Sample US773 is  
188 chloritoid-richer than sample US900 and contains abundant Mg-chlorite, derived from chloritoid  
189 retrogression (vol%: Qz 21, Tlc 22, Cld 23, Mg-Chl 23, Gln 3, Grt 8) (Fig. 3 and Table 3). Although rich  
190 in talc, these rocks do not show a pervasive schistosity, due to the presence of garnet, chloritoid and  
191 glaucophane porphyroblasts up to few millimetre in size, which partially obliterate the oriented  
192 structure.

193 Chloritoid occurs as bluish-green, slightly zoned, porphyroblasts, with a darker core and a  
194 lighter rim (Fig. 4f). It is locally pervasively replaced by a greenish Mg-chlorite, especially in sample  
195 US773. Its  $X_{Mg}$  ranges from 0.29 in the core to 0.38 in the rim, whereas  $X_{Fe^{+3}}$  is slightly higher in the  
196 core than in the rim (core:  $X_{Fe^{+3}} = 0.05-0.08$ ; rim:  $X_{Fe^{+3}} = 0.04-0.07$ ) (Fig. 5d and Table 2)  
197 [ $X_{Mg} = Mg/(Mg+Fe)$ ;  $X_{Fe^{+3}} = Fe^{+3}/(Fe^{+3}+Al)$ ].

198 Garnet porphyroblasts are idioblastic and strongly zoned (Fig. 4a-d), with a reddish core  
199 ( $X_{Fe} = 0.73-0.79$ ,  $X_{Mg} = 0.07-0.09$ ,  $X_{Mn} = 0.05-0.12$ ,  $X_{Ca} = 0.08-0.10$ ), a pink mantle ( $X_{Fe} = 0.79-0.83$ ,  $X_{Mg} = 0.09-$   
200  $0.12$ ,  $X_{Mn} = 0.01-0.04$ ,  $X_{Ca} = 0.05-0.08$ ) and a colourless rim ( $X_{Fe} = 0.76-0.79$ ,  $X_{Mg} = 0.13-0.29$ ,  $X_{Mn} = 0.00-$   
201  $0.01$ ,  $X_{Ca} = 0.04-0.06$ ) (Table 1, Fig. 6a and Fig. S1, freely available online as Supplementary Material  
202 linked to this article on the GSW website of the journal, <http://eurjmin.geoscienceworld.org/>). The  
203 bell-shaped profile of Mn suggests a prograde garnet growth (Fig. 6b). Similarly to Mn, Y, Cr and Na  
204 contents also show a bell-shaped profile (Fig. 6b). Maximum Y, Na and Cr contents in garnet core are  
205 2000, 730, and 480 ppm, respectively, and decreases to almost zero in garnet rim. P has an opposite  
206 trend: it is almost absent in garnet core and increases toward the rim, up to 220 ppm.

207 The garnet core and mantle includes chloritoid ( $X_{Mg} = 0.21-0.24$ ;  $X_{Fe^{+3}} = 0.07-0.10$ ) (Fig. 6d and  
208 Fig. S1), very rare and fine-grained phengite (Si = 3.30 a.p.f.u. on the basis of 11 oxygens) locally  
209 associated to chloritoid, and rare ilmenite (especially in the garnet core). The garnet mantle and rim  
210 preserves relict coesite, partially inverted to quartz (Fig. 4c,d and Fig. S1). The garnet rim locally  
211 includes talc, whereas fine-grained rutile is ubiquitous as inclusion in garnet.

212 Coesite inclusions preserved in garnet mantle are quite big (up to 200  $\mu m$ ) and poorly  
213 retrogressed to quartz (Fig. 7a), compared to coesite included in garnet rim, that is mostly replaced  
214 by quartz with a palisade structure (Fig. 7b) or by polycrystalline quartz (Fig. 7a). Garnet surrounding  
215 the coesite inclusions shows the typical radial fractures due to the volume increase related to the  
216 coesite-quartz inversion (Fig. 4c,d; Fig. 7b). The presence of coesite is confirmed by micro-Raman  
217 analyses on exposed inclusions (Fig. 7c), which show the typical coesite vibrations (Frezzotti *et al.*,

218 2011). The upshift of most, but not all, of coesite peaks (e.g., the main peak at  $523\text{ cm}^{-1}$  instead of  
219  $521\text{ cm}^{-1}$ ) indicates that a residual pressure is still preserved in the inclusions (e.g., Korsakov *et al.*,  
220 2007; Khon, 2014). The best preserved, although exposed, single coesite inclusion has been selected  
221 for Raman mapping (Fig. 7d). Also this coesite preserves a residual pressure (main peak at  $524\text{ cm}^{-1}$ ).  
222 Quartz is optically detectable only in two cracks crosscutting the inclusion (Fig. 7d). Raman map (Fig.  
223 7e) confirms the presence of quartz along the cracks, but also reveals the distribution of optically  
224 undetectable quartz (i) as thin shell of  $1\text{-}5\text{ }\mu\text{m}$  in thickness that completely surrounds the coesite  
225 inclusion, and (ii) as thin veinlets ( $<5\text{ }\mu\text{m}$  in thickness) cutting the coesite. The main peak of quartz at  
226  $470\text{ cm}^{-1}$  instead of  $464\text{ cm}^{-1}$  indicates an high residual pressure due to the coesite-to-quartz  
227 transition (e.g., Korsakov *et al.*, 2009). These data confirm that the initial stage of inversion from  
228 coesite to quartz subgrains occurs at grain boundaries between coesite and hosting garnet, and along  
229 crosscutting cracks (e.g., Korsakov *et al.*, 2007).

230 A slightly-zoned, bluish to colourless glaucophane (abundant in sample US900: Fig. 3, 4a) is in  
231 equilibrium with both chloritoid (Fig. 4e) and garnet rims and with talc. Its  $X_{\text{Mg}}$  and  $X_{\text{Fe}+3}$  are slightly  
232 variable from core to rim (core:  $X_{\text{Mg}} = 0.70\text{-}0.74$ ,  $X_{\text{Fe}+3} = 0.20\text{-}0.33$ ; rim:  $X_{\text{Mg}} = 0.72\text{-}0.76$ ,  $X_{\text{Fe}+3} = 0.14\text{-}$   
233  $0.23$ ) (Fig. 5a-c and Table 2). In the more retrograded sample US773, glaucophane is locally  
234 surrounded by a thin and discontinuous rim of Na-Ca amphibole (winchite).

235 Talc has a  $X_{\text{Mg}}=0.85\text{-}0.88$  (Table 2). Mg-chlorite is a late phase, developed at the expenses of  
236 chloritoid in sample US7773 (Fig. 4b, f). Its composition is quite homogeneous, with a  $X_{\text{Mg}} = 0.60\text{-}0.71$   
237 (Table 2). Very rare epidote has also been observed in sample US773, and seems in equilibrium with  
238 Mg-chlorite.

239

#### 240 **4. Phase equilibria and P-T evolution**

##### 241 **4.1 Stability field of the chloritoid + glaucophane + garnet $\pm$ talc assemblage: previous studies**

242 Chloritoid + glaucophane  $\pm$  garnet and chloritoid + garnet + talc  $\pm$  glaucophane assemblages are  
243 typical of blueschists and low-T eclogites in high-pressure terranes around the world. The  
244 coexistence of chloritoid + glaucophane  $\pm$  garnet is reported in metapelitic rocks from the Variscan  
245 Ile de Groix (Kienast & Triboulet, 1972; Bosse *et al.*, 2002), Vendée (Guiraud *et al.*, 1987) and Iberian  
246 Massif (Lopez-Carmona *et al.*, 2010), the Gran Paradiso Massif of the western Alps (Chopin, 1981),  
247 the Peloponnese in Greece (Katagas, 1980; Theye & Seidel, 1991), Turkey (Okay, 2002), Oman (El-  
248 Shazly & Liou, 1991; Warren & Waters, 2006), New Caledonia (Ghent *et al.*, 1987), Sulawesi in  
249 Indonesia (Miyazaki *et al.*, 1996), and the Chinese Tianshan (Wei *et al.*, 2009) and Qilian orogens (Wei  
250 & Song, 2008).

251 Talc + chloritoid  $\pm$  garnet  $\pm$  glaucophane assemblages, similar to that observed in the studied  
252 samples, are more rarely reported. They were described from the Gran Paradiso and Monte Rosa  
253 Massifs of the western Alps (silvery micaschist: Compagnoni & Lombardo, 1974; Chopin, 1981;  
254 Chopin & Moniè, 1984; Dal Piaz & Lombardo, 1986; Goffè & Chopin, 1986; Meffan-Main *et al.*, 2004;  
255 Gabudianu Radulescu *et al.*, 2009), the Chinese Qilian orogen (Wei & Song, 2008) and the Tianshan of  
256 Kazakhstan and Kyrgyzstan (Meyer *et al.*, 2014; Klemd *et al.*, 2015; Orozbaev *et al.*, 2015). This last  
257 occurrence is worth of note, because of the presence of coesite relicts included in garnet.

258 Thermodynamic calculations in the model system NFMASH, NKFMAH and NCKFMASH (e.g.  
259 Guiraud *et al.*, 1990; Proyer, 2003; Wei & Powell, 2004, 2006) suggested that the chloritoid +  
260 glaucophane  $\pm$  garnet assemblage is a high-pressure indicator in metapelites, being stable at  
261 pressures higher than 18-19 kbar (except for Fe-rich compositions, where this assemblage is stable at  
262 pressures as lower as 7-8 kbar: Wei & Song, 2008). The maximum stability field of the chloritoid +



263 glaucophane ± garnet assemblage is constrained at P = 19-35 kbar and T = 420-610 °C. In the quartz  
264 stability field, this assemblage provides tight temperature constraints, being limited by the  
265 appearance of the carpholite + jadeite assemblage at temperatures lower than ca. 420-430 °C and by  
266 the appearance of garnet + kyanite + talc at temperature higher than ca. 600-610 °C. At pressures  
267 above the quartz-coesite transition, the high-T boundary of this assemblage is still located at about  
268 600 °C, whereas the low-T boundary is more P-dependent resulting in a field assemblage  
269 progressively narrower toward high-P (Proyer, 2003; Wei & Powell, 2004, 2006). Furthermore,  
270 chloritoid + glaucophane ± garnet assemblage is easily preserved during exhumation because it  
271 requires external hydration in order to breakdown to lower pressures (Proyer, 2003).

272 The addition of talc results in a further limitation of the talc + chloritoid + glaucophane +  
273 garnet stability field, limited at lower temperatures by the appearance of carpholite + chlorite/garnet  
274 at about 530-550°C. This assemblage is predicted to be stable also at ultra-high pressure conditions,  
275 in the narrow temperature range of about 550-600°C for P < 35 kbar (Proyer, 2003; Wei & Powell,  
276 2004, 2006; Franz *et al.*, 2013).

277

#### 278 **4.2 Thermodynamic modelling of the chloritoid + glaucophane + garnet + talc stability field**

279 The prograde P-T evolution of the less retrograded sample US900 has been constrained using two  
280 different pseudosections calculated in the MnNCFMASHO model system, considering the  
281 fractionation effects due to the growth of garnet porphyroblasts: (i) a first pseudosection, calculated  
282 using the whole rock composition, has been used to model the growth of garnet core (Fig. 8a); (ii) a  
283 second pseudosection, calculated using the effective bulk composition derived by subtracting garnet  
284 cores and mantles to the whole rock composition, has been used to model the growth of garnet rim  
285 (Fig. 8b).

286 The topologies of both pseudosections are very similar. The observed talc + chloritoid +  
287 glaucophane + garnet assemblage is predicted to be stable in a quite small field. This field  
288 assemblage is limited toward lower pressure and temperature by the presence of chlorite instead of  
289 talc, toward higher pressure by the presence of carpholite instead of chloritoid and toward higher  
290 temperature by the presence of kyanite instead of chloritoid (Fig. S2); furthermore, it extends up to  
291 ca. 31 kbar, in the coesite-stability field (Fig. 8a,b). The dimension of the coesite + talc + chloritoid +  
292 glaucophane + garnet field assemblage is mainly controlled by the carpholite-in and kyanite-in  
293 trivariant reactions.

294 The position of the carpholite-in field boundary is critically dependent on the carpholite  
295 thermodynamic parameters used in the calculation; it is worth of note that the topology of Fig. 8a,b  
296 has been obtained using the most recent Holland & Powell (2011) database, whereas using older  
297 versions of the same database, the coesite + talc + chloritoid + glaucophane + garnet field  
298 assemblage is predicted to be stable in a narrower P-T field (Holland & Powell, 1998) or it is not  
299 predicted to be stable at all (Holland & Powell, 1998, updated 2004; i.e. the talc + chloritoid +  
300 glaucophane + garnet assemblage is only stable in the quartz stability field). The carpholite  
301 thermodynamic parameters and, consequently, its stability field, have been a matter of debate in the  
302 past (e.g. Vidal & Theye, 1996) and it is plausible that they are still not very well constrained.  
303 However, the results obtained using the Holland & Powell (2011) database are in very good  
304 agreement with the observed equilibrium assemblage and we are therefore confident that the  
305 thermodynamic parameters of carpholite are now quite well calibrated.

306

#### 307 **4.3 P-T evolution**

308 The pseudosection calculated using the whole rock bulk composition allowed to constrain the P-T  
309 conditions for the growth of garnet core. Garnet core is predicted to grow in the quartz stability field,  
310 at  $T > 450$  °C, through chlorite breakdown (Fig. 8a). The modelled garnet and chloritoid  
311 compositional isopleths [ $X_{Mg}(Grt)=0.08$ ;  $X_{Ca}(Grt)=0.09$ ;  $X_{Mn}(Grt)=0.12$ ;  $X_{Mg}(Cld)=0.29$ ] constrain the  
312 growth of garnet core at ca. 450-480°C, 22-26 kbar, in the chlorite + glaucophane + garnet +  
313 chloritoid + quartz + lawsonite field (lawsonite < 0.1 vol%; Fig. S2) (Fig. 8a). These temperature  
314 conditions are in very good agreement with the results obtained using the YAG thermometer (Pyle &  
315 Spear, 2000) applied on the maximum Y content measured in the garnet cores (i.e. 2000 ppm), which  
316 gives a maximum temperature of 496 °C.

317 P-T conditions for the growth of garnet rim have been constrained using the pseudosection  
318 calculated using the fractionated composition obtained by subtracting garnet cores and mantles to  
319 the whole rock bulk composition. The main differences between the two pseudosections is the shift  
320 of the garnet-in curve toward higher T and P for the fractionated pseudosection (Fig. 8b). The  
321 modelled garnet and chloritoid compositional isopleths [ $X_{Mg}(Grt)=0.20$ ;  $X_{Ca}(Grt)=0.04$ ;  $X_{Mn}(Grt)=0.00$ ;  
322  $X_{Mg}(Cld)=0.37$ ] constrain the growth of garnet core at ca. 480-510°C, 25-31 kbar, in the talc +  
323 chloritoid + glaucophane + garnet + quartz/coesite field. The occurrence of coesite still preserved in  
324 garnet rim further constrain the P-T conditions of garnet rim at 480-510°C, 27-31 kbar (Fig. 8b).  
325 Finally, the modelled isomodes predicts the following modal abundances at the estimated peak P-T  
326 conditions: Coe36, Tlc29, Cld14, Gln12, Grt9 (vol%) (Fig. 8c-i), which are in very good agreement with  
327 the observed modal proportions of the main mineral phases.

328 Overall, the P-T evolution resulting from the thermodynamic modelling and thermometric  
329 results is characterized by a prograde increase in both pressure and temperature from ca. 460 °C, 25  
330 kbar to ca. 510 °C, 28 kbar, just above the quartz to coesite transition (Fig. 9). The obtained results  
331 also suggest the crucial role of the quartz-consuming reaction  $Chl + Qz \rightarrow Cld + Grt + Tlc$  for the  
332 formation of the observed equilibrium assemblage.

333 In sample US900, the retrogression effects are very scarce. The modelled H<sub>2</sub>O isomodes show  
334 that, during exhumation, the system was H<sub>2</sub>O under-saturated whatever decompression path was  
335 followed (either isobaric or cooling decompression) (Fig. 8l). This means that metamorphic reactions  
336 could not proceed until H<sub>2</sub>O-saturated conditions were again reached or, alternatively, H<sub>2</sub>O was  
337 introduced from outside (see Guiraud *et al.*, 2001 for the interpretation of H<sub>2</sub>O-saturated vs. H<sub>2</sub>O-  
338 undersaturated conditions), and explains why the UHP assemblage remained preserved. On the  
339 opposite, in sample US773, chlorite pervasively grew at the expenses of chloritoid, glaucophane is  
340 locally rimmed by a discontinuous rim of NaCa-amphibole, and small epidote granoblasts  
341 occasionally occur in the rock matrix. This incipient retrogression can only be justified by the addition  
342 of a low H<sub>2</sub>O amount from outside the system.

343

## 344 5. Discussion

### 345 5.1 Petrogenesis of the coesite-bearing chloritoid + garnet + glaucophane talcschists

346 The equilibrium assemblage observed in the studied rocks reflects a quite unusual Mg-rich  
347 composition that requires further discussion as concerning the possible protolith and the genetic  
348 processes involved in their formation. The studied talcschists can be described in a slightly oxidized  
349 MgO-FeO-Al<sub>2</sub>O<sub>3</sub>-SiO<sub>2</sub>-H<sub>2</sub>O system with low amounts of Na<sub>2</sub>O (< 1 wt%) and CaO (< 0.3 wt%) (Table 3).  
350 They are not “whiteschist” *sensu stricto* because, according to the official nomenclature, they should  
351 contain the assemblage talc + kyanite (or the UHP equivalent pyrope + kyanite) (Fettes & Desmons,  
352 2007), whereas the term “silvery micaschist”, used for similar chloritoid ± garnet ± phengite

353 talcschists can be applied (e.g. Compagnoni & Lombardo, 1974; Meffan-Main *et al.*, 2004; Gabudianu  
354 Radulescu *et al.*, 2009). Beside the high amount of MgO, they are characterized by significant  
355 amounts of FeO<sub>tot</sub> (up to 16 wt%) and are completely devoid of K<sub>2</sub>O (Table 3).

356 Possible protoliths with a composition suitable to develop the observed equilibrium  
357 assemblage are: (1) Mg-rich rocks of either sedimentary or volcanic nature, and (2) metasomatically  
358 altered felsic or mafic rocks (see Franz *et al.*, 2013 for a discussion of the protoliths of whiteschists  
359 and Ferrando, 2012 for a review on Mg-metasomatism of metagranitoids). The lack of field data and  
360 of any information regarding the location of the ancient quarry from where these quern-stones were  
361 extracted hampers a definitive interpretation of the protolith and of the genetic processes  
362 responsible for the formation of the observed assemblage. However, because the site of the retrieval  
363 of the quern-stones clearly points to a provenience of these rocks from the southern Dora-Maira  
364 Massif, some speculations can be proposed.

365

### 366 **5.1.1 Mg-rich protoliths metamorphosed in a closed-system**

367 Franz *et al.* (2013) demonstrated that pre- or syn-metamorphic metasomatism is not an essential  
368 prerequisite for the formation of Mg-rich and alkali-poor assemblages. Both weathered or  
369 hydrothermally altered volcanic rocks and Mg-rich sedimentary protoliths can have a composition  
370 suitable to develop talc-bearing assemblages. Among sedimentary protoliths, the best candidates are  
371 palygorskite-rich clays deposited in continental lacustrine or in shallow marine environments, and  
372 sepiolite, illite and/or smectite-rich pelitic rocks from evaporitic successions deposited in  
373 epicontinental marine settings (see also Kulke & Schreyer, 1976; Schreyer, 1977; Moine *et al.*, 1981).

374 Although in principle a non-metasomatic origin cannot be excluded for the studied samples,  
375 similar protoliths are unknown so far in the southern Dora-Maira Massif, which mainly consists of a  
376 Variscan metamorphic basement (i.e. mainly amphibolite-facies metapelites with minor lenses of  
377 metabasics and marbles) intruded by Permian granitoids.

378

### 379 **5.1.2 Felsic or mafic protoliths metamorphosed in an open-system (i.e. metasomatic protoliths)**

380 Although the chemical weathering could be locally responsible for the Mg-metasomatism of the  
381 protolith of a HP-UHP rock (e.g., Franz *et al.*, 2013), in an orogenic setting such as the Alps many  
382 other pervasive Mg-metasomatic processes widely occur and are more suitable to produce small  
383 volumes (layers, lens-like bodies, veins, etc.) of Mg-metasomatic rocks. Ferrando (2012) discussed  
384 the metasomatic processes responsible for the transformation of alkali-rich metagranitoids into Mg-  
385 rich and alkali-poor metasomatic schists in the Alps, and demonstrated that these processes were  
386 widespread and can be ascribed to different tectonic settings that were active at different times.  
387 From this review, the most common Mg-metasomatic process that affected the continental crustal  
388 rocks of the Alps along shear zones results to be the pervasive influx of Mg-rich, highly channelized  
389 fluids derived from ultramafics previously interacting with seawater. This process can occur during  
390 the rift-related ocean-continent transition, the continental subduction and/or the continent-  
391 continent collision. The metasomatic products are typically characterized by strong depletions in  
392 alkalis (very low or even null K<sub>2</sub>O and Na<sub>2</sub>O contents) and low depletions in silica, and by strong  
393 enrichments in MgO (+ minor NiO<sub>2</sub> and/or Cr<sub>2</sub>O<sub>3</sub>) and by variable enrichments in FeO<sub>tot</sub> depending on  
394 the initial composition of the protolith. Mg-metasomatic rocks formed at the expenses of granitic  
395 protoliths (e.g. the well-known pyrope-bearing whiteschists of the Brossasco-Isasca Unit; Ferrando *et al.*,  
396 2009) are low in FeO<sub>tot</sub> (< 2 wt%), whereas those formed at the expenses of granodioritic  
397 protoliths are significantly richer in FeO<sub>tot</sub>. For example, chlorite + garnet + staurolite schists (almost  
398 free of quartz) with up to ca. 19 wt% of FeO<sub>tot</sub>, but with low Na<sub>2</sub>O (< 0.5 wt%) and SiO<sub>2</sub> (< 32 wt%)

399 and relatively high CaO (> 0.7 wt%) and K<sub>2</sub>O (> 3.5 wt%), are described as the final metasomatic  
400 product of a metagranodiorite from the Tauern window of eastern Alps (Selverstone *et al.*, 1991;  
401 Barnes *et al.*, 2004).

402 Meyer *et al.* (2014) described coesite-bearing garnet + chloritoid talcschists with mineral  
403 assemblage and compositions similar to those described in this study, but with a significantly lower  
404 modal amount of quartz (< 5 vol%) and lacking of glaucophane. Because the field evidence shows  
405 that the talcschists envelop blocks and boudins of mafic oceanic rocks tectonically embedded in  
406 continentally derived metasediments, these Authors interpreted the talcschists as the metasomatic  
407 product of a mafic protolith (either hydrothermally altered oceanic crust or volcanoclastic rock). Also  
408 these talcschists are characterized by high FeO<sub>tot</sub> contents (FeO<sub>tot</sub> = 20 wt%) and very low alkalis, but  
409 show a low SiO<sub>2</sub> content (45 wt%).

410 Both these two protoliths, i.e. granitoids and strongly altered mafic rocks, can be reasonably  
411 excluded for the studied rocks. The studied talcschists cannot derive from a Fe-rich metagranitoid,  
412 i.e. a metagranodiorite, because the amounts of Na<sub>2</sub>O and SiO<sub>2</sub> are too high and those of CaO and  
413 K<sub>2</sub>O are too low compared with the previously documented examples of metasomatic granodiorites  
414 (Selverstone *et al.*, 1991; Barnes *et al.*, 2004). Moreover, metagranodiorites, or chemically equivalent  
415 orthogneisses, are not reported in the southern Dora-Maira Massif (e.g. Compagnoni *et al.*, 2012 and  
416 references therein). Similarly, a protolith consisting of altered oceanic crust or altered volcanoclastic  
417 rocks, is not compatible with the bulk of the studied rocks and is not coherent with the tectonic  
418 setting of the southern Dora-Maira Massif (e.g. Compagnoni *et al.*, 2012).

419 One of the quern-stone associated to those carved from the talcschists is carved from a  
420 garnet + chloritoid + glaucophane phengitic schist (Fig. S3), i.e. a widespread lithology outcropping in  
421 the Rocca-Solei Unit (e.g. Compagnoni & Rolfo, 2003; Compagnoni *et al.*, 2012). Although we cannot  
422 prove that this quern-stone was extracted from the same locality of the studied coesite + chloritoid +  
423 garnet ± glaucophane talcschists, we can speculate that this lithology might represent the most  
424 credible non-metasomatized equivalent of the talcschists. If it is the case, the Mg-metasomatism  
425 could have moderately affected a “common” Fe-rich metapelite such as those that constitute the  
426 majority of the Variscan basement in the southern Dora-Maira Massif.

427 Regarding the kind of metasomatism and its timing, the relatively high Cr content in garnet  
428 points to the involvement of mantle derived fluids, and both microstructural relationships and  
429 minerochemical data point to a process occurred before the garnet growth (i.e. at P < 25 kbar). In  
430 fact, the Cr concentration decreases from garnet core to rim (Fig. 6b), opposite to what would be  
431 expected if a Mg-rich, mantle derived, metasomatic fluid was introduced in the system after the  
432 growth of garnet core (e.g. Ferrando *et al.*, 2009). This implies that the metasomatic process could  
433 have occurred during early subduction, such as occurred for the well-known pyrope-bearing  
434 whiteschists in the UHP Brossasco-Isasca Unit (Ferrando *et al.*, 2009), i.e. by a prograde influx of  
435 antigorite-derived fluids along shear zones. However, as an alternative process, the metasomatism  
436 could have occurred during the opening of the Tethyan basin, when fluids derived from hydrated  
437 ultramafic rocks could have infiltrated the continental crust along rift-related detachment systems  
438 (Ferrando, 2012).

439

## 440 **5.2 Possible evidence for a new UHP unit in the southern Dora-Maira Massif**

441 The location of the *villa rustica* and the occurrence of coesite relics, might have suggested the  
442 obvious conclusion that the studied talcschists come from the nearby UHP Brossasco-Isasca Unit  
443 (BIU), which is only ca. 5 km from Costigliole Saluzzo (Fig. 1a). However, the results of  
444 thermodynamic modelling clearly show that the studied talcschists experienced peak P-T conditions

445 at UHP conditions, but at significant lower temperature (and pressure) than the BIU (Fig. 9). In the  
446 western Alps, the only other UHP unit known so far is the Lago di Cignana Unit (e.g. Reinecke, 1991;  
447 Groppo *et al.*, 2009; Frezzotti *et al.*, 2011), located in the Internal Piemontese Zone (Zermatt-Saas  
448 Zone) of the upper Valtournanche, ca. 150 km from Costigliole Saluzzo. The calculated P-T conditions  
449 for the prograde and peak stages do not match with the P-T path obtained for the Lago di Cignana  
450 Unit (Groppo *et al.*, 2009) and it can be, therefore, excluded that the quern-stones come from there.

451 The high number of quern-stones carved from garnet + chloritoid + glaucophane talcschist  
452 and phengitic schists unearthed in the *villa rustica* suggests that they were not realized starting from  
453 a small outcrop or block occasionally found in the surroundings, but that a small quarry should have  
454 existed, likely set in correspondence of a talcschist horizon (thick at least few meters and with a good  
455 lateral continuity) possibly within the phengitic schists of the Rocca-Solei Unit. Coesite relics have  
456 been never reported so far from this Unit; however, the Rocca-Solei Unit has been significantly less  
457 studied than the BIU (the last petrological works date back to more than 15 years ago: Chopin *et al.*,  
458 1991; Matsumoto & Hirajima, 2000) and it is possible that a systematic search for UHP evidence  
459 could led to new coesite findings in the next future.

460 Further fieldwork and petrological investigation are therefore required in order to confirm  
461 (or disprove) the existence of a second UHP unit in the southern Dora-Maira Massif. Such a discovery  
462 could potentially have important implications for the understanding of the subduction and  
463 exhumation processes that were active in convergent settings and that were responsible for the  
464 actual architecture of the Alpine chain.

465

#### 466 **Acknowledgements**

467 We gratefully acknowledge Roberto Compagnoni for being a constant source of inspiration and for  
468 sharing his longstanding experience: we are indebted to him for most of our knowledge about the  
469 southern Dora-Maira Massif.

470 Raman analytical facilities were provided by the Interdepartmental Center "G. Scansetti" and by the  
471 Compagnia di San Paolo, Torino, Italy.

472 **References**

- 473 Barnes, J.D., Selverstone, J., Sharp, Z.D. (2004): Interactions between serpentinite devolatilization,  
474 metasomatism and strike-slip strain localization during deep-crustal shearing in the Eastern Alps. *J.*  
475 *Metamorph. Geol.*, **22**, 283–300.
- 476 Bosse, V., Balleuvre, M., Vidal, O. (2002): Ductile thrusting recorded by the garnet isograd from  
477 blueschist-facies metapelites of the Ile de Groix, Armorican Massif, France. *J. Petrol.*, **43**, 485–510.
- 478 Castelli, D., Compagnoni, R., Lombardo, B. Angiboust, S., Balestro, G., Ferrando, S., Groppo, C.,  
479 Hirajima, T., Rolfo, F. (2014): Crust-mantle interactions during subduction of oceanic & continental  
480 crust. 10th International Eclogite Conference, Courmayeur (Aosta, Italy): Post-conference  
481 excursions: September 9-10, 2013. *Geological Field Trips*, **6 (1.3)**, 73 pp.
- 482 Chopin, C., Henry, C., Michard, A. (1991): Geology and petrology of the coesite-bearing terrain, Dora  
483 Maira massif, Western Alps. *Eur. J. Mineral.*, **3**, 263–291.
- 484 Chopin, C. & Monié, P. (1984): A unique magnesiochloritoid-bearing, high-pressure assemblage from  
485 the Monte Rosa, Western Alps: petrologic and <sup>40</sup>Ar/<sup>39</sup>Ar radiometric study. *Contrib. Mineral. Petrol.*,  
486 **87**, 388–398.
- 487 Chopin, C. (1981): Talc-phengite: a widespread assemblage in high-grade pelitic blueschists of the  
488 Western Alps. *J. Petrol.*, **22**, 628–650.
- 489 Compagnoni, R. & Rolfo, F. (2003): Ultrahigh-pressure units in the Western Alps. *in*: “Ultrahigh-  
490 pressure metamorphism”, D.A. Carswell & R. Compagnoni, eds., EMU Notes in Mineralogy, 5, 13–  
491 49.
- 492 Compagnoni, R., Rolfo, F., Groppo, C., Hirajima, T., Turello, R. (2012): Geologic map of the UHP  
493 Brossasco-Isasca Unit (Western Alps). *J. Maps*, **8**, 465–472.
- 494 Compagnoni, R. & Lombardo, B. (1974): The Alpine age of the Gran Paradiso eclogites. *Rend. Soc. It.*  
495 *Mineral. Petrol.*, **30**, 223–237.
- 496 Connolly, J.A.D. (2009): The geodynamic equation of state: what and how. *Geochem. Geophys.*  
497 *Geosyst.*, **10**, Q10014.
- 498 Connolly, J.A.D. (1990): Multivariable phase diagrams: an algorithm based on generalized  
499 thermodynamics. *Am. J. Sci.*, **290**, 666–718.
- 500 Cossio, R., Borghi, A., Ruffini, R. (2002): Quantitative modal determination of geological samples  
501 based on X-ray multielemental map acquisition. *Microsc. Microanal.*, **8**, 139–149.
- 502 Dal Piaz, G. & Lombardo, B. (1986): Early Alpine eclogite metamorphism in the Penninic Monte Rosa-  
503 Gran Paradiso basement nappes of the northwestern Alps. *Geol. Soc. Am. Bull.*, **164**, 249–265.
- 504 Dale, J., Holland, T., Powell, R. (2000): Hornblende-garnet-plagioclase thermobarometry: a natural  
505 assemblage calibration of the thermodynamics of hornblende. *Contrib. Mineral. Petrol.*, **140**, 353–  
506 362.
- 507 Diener, J.F.A. & Powell R. (2011): Revised activity–composition models for clinopyroxene and  
508 amphibole. *J. Metamorph. Geol.*, **30**, 131–142.
- 509 Donner, M. & Marzoli, C. (1994): La macinazione. Evoluzione delle tecniche e degli strumenti. *In*: “Il  
510 grano e le macine: la macinazione di cereali in Alto Adige, dall’Antichità al Medioevo”, S. de  
511 Rachewiltz, L. Dal Ri, C. Marzoli, eds., Castel Tirolo, 73-93.
- 512 Elia, D. & Meirano, V. (2012): La villa di Costigliole Saluzzo (CN). Contributo alla conoscenza del  
513 territorio piemontese in età romana. *Orizzonti. Rassegna di Archeologia*, **XIII**, 43–65.
- 514 Elia, D., Meirano, V., Russo, D. (2013): Costigliole Saluzzo, località Cimitero. Insediamento di età  
515 romana. Interventi di scavo e di restauro: campagna 2012. *Quaderni della Soprintendenza*  
516 *Archeologica del Piemonte*, **28**, 220–223.

517 El-Shazly, A.E.D.K. & Liou, J.G. (1991): Glaucophane-chloritoid-bearing assemblages from NE Oman:  
518 petrologic significance and petrogenetic grid for high P metapelites. *Contrib. Mineral. Petrol.*, **107**,  
519 180–201.

520 Ferrando, S. (2012): Mg-metasomatism of metagranitoids from the Alps: genesis and possible  
521 tectonic scenarios. *Terra Nova*, **24**, 423 *Contrib. Mineral. Petrol.*, 436.

522 Ferrando, S., Frezzotti, M.L., Petrelli, M., Compagnoni, R. (2009): Metasomatism of continental crust  
523 during subduction: the UHP whiteschists from the Southern Dora-Maira Massif (Italian Western  
524 Alps). *J. Metamorph. Geol.*, **27**, 739–756.

525 Fettes, D. & Desmons, J. (2007): Metamorphic rocks. A Classification and Glossary of Terms.  
526 Recommendations of the International Union of Geological Sciences Subcommittee on the  
527 Systematics of Metamorphic Rocks. Cambridge University Press, Cambridge, 244 pp.

528 Franz, L., Romer, R.L., de Capitani, C. (2013): Protoliths and phase petrology of whiteschists. *Contrib.*  
529 *Mineral. Petrol.*, **166**, 255–274.

530 Frezzotti, M.L., Selverstone, J., Sharp, Z.D., Compagnoni, R. (2011): Carbonate dissolution during  
531 subduction revealed by diamond-bearing rocks from the Alps. *Nat. Geosci.*, **4**, 703–706.

532 Frezzotti, M.L., Tecce, F., Casagli, A. (2011): Raman spectroscopy for fluid inclusion analysis. *J.*  
533 *Geochem. Explor.*, **112**, 1–20.

534 Gabudianu Radulescu, I., Rubatto, D., Gregory, C., Compagnoni, R. (2009): The age of HP  
535 metamorphism in the Gran Paradiso Massif, Western Alps: a petrological and geochronological  
536 study of “silvery micaschists”. *Lithos*, **110**, 95–108.

537 Ghent, E.D., Stout, M.Z., Black, P.M., Brothers, R.N. (1987): Chloritoid-bearing rocks associated with  
538 blueschists and eclogites, northern New Caledonia. *J. Metamorph. Geol.*, **5**, 239–254.

539 Goffé, B. & Chopin, C. (1986): High-pressure metamorphism in the Western Alps: zoneography of  
540 metapelites, chronology and consequences. *Schweiz. Mineral. Petrog. Mitt.*, **66**, 41–52.

541 Groppo, C., Beltrando, M., Compagnoni, R. (2009): P-T path of the UHP Lago di Cignana and adjoining  
542 HP meta-ophiolitic units: insights into the evolution of subducting tethyan slab. *J. Metamorph.*  
543 *Geol.*, **27**, 207–231.

544 Guiraud, M., Burg, J.P., Powell, R. (1987): Evidence for a Variscan suture zone in the Vendée, France:  
545 a petrological study of blueschist facies rocks from Bois de Cene. *J. Metamorph. Geol.*, **5**, 225–237.

546 Guiraud, M., Holland, T., Powell, R. (1990): Calculated mineral equilibria in the greenschist-  
547 blueschist-eclogite facies in Na<sub>2</sub>O-FeO-MgO-Al<sub>2</sub>O<sub>3</sub>-SiO<sub>2</sub>-H<sub>2</sub>O. *Contrib. Mineral. Petrol.*, **104**, 85–98.

548 Guiraud, M., Powell, R., Rebay, G. (2001): H<sub>2</sub>O in metamorphism and unexpected behaviour in the  
549 preservation of metamorphic mineral assemblages. *J. Metamorph. Geol.*, **19**, 445–454.

550 Holland, T.J.B. & Powell, R. (2011): An improved and extended internally consistent thermodynamic  
551 dataset for phases of petrological interest, involving a new equation of state for solids. *J.*  
552 *Metamorph. Geol.*, **29**, 333–383.

553 Holland, J.T.B., Baker, J., Powell, R. (1998): Mixing properties and activity-composition relationships  
554 of chlorites in the system MgO-FeO-Al<sub>2</sub>O<sub>3</sub>-SiO<sub>2</sub>-H<sub>2</sub>O. *Eur. J. Mineral.*, **10**, 395–406.

555 Katagas, C. (1980): Ferrograucophane and chloritoid-bearing metapelites from the phyllite series,  
556 southern Peloponnese, Greece. *Mineral. Mag.*, **43**, 975–978.

557 Kiénast, J.R. & Triboulet, C. (1972): Le chloritoïde dans les paragenèses à glaucophane, albite ou  
558 paragonite. *Bull. Soc. Franc. Minéral. Cristall.*, **95**, 565–573.

559 Klemd, R., Gao, J., Li, J.-L., Meyer, M. (2015): Metamorphic evolution of (ultra)-high-pressure  
560 subduction-related transient crust in the South Tianshan Orogen (Central Asian Orogenic Belt):  
561 Geodynamic implications. *Gondw. Res.*, **28**, 1–25.

562 Kohn, M.J. (2014): "Thermobarometry": Calibration of spectroscopic barometers and  
563 thermometers for mineral inclusions. *Earth Planet. Sci. Lett.*, **388**, 187-196.

564 Korsakov, A.V., Hutsebaut, D., Theunissen, K., Vandenabeele, P., Stepanov, A.S. (2007): Raman  
565 mapping of coesite inclusions in garnet from the Kokchetav Massif (Northern Kazakhstan).  
566 *Spectrochim. Acta Part A*, **68**, 1046-1052.

567 Korsakov, A.V., Perraki, M., Zhukov, V.P., De Gussem, K., Vandenabeele, P., Tomilenko, A.A. (2009): Is  
568 quartz a potential indicator of ultrahigh-pressure metamorphism? Laser Raman spectroscopy of  
569 quartz inclusions in ultrahigh-pressure garnets. *Eur. J. Mineral.*, **21**, 1313-1323.

570 Kulke, H. & Schreyer, W. (1973): Kyanite-talc-schist from Sar E Sang, Afghanistan. *Earth Planet. Sci.*  
571 *Lett.*, **18**, 324-328.

572 Lopez-Carmona, A., Abati, J., Reche, J. (2010): Petrologic modeling of chloritoid-glaucophane schists  
573 from the NW Iberian Massif. *Gondw. Res.*, **17**, 377-391.

574 Matsumoto, N. & Hirajima, T. (2000): Garnet in pelitic schists from a quartz-eclogite unit in the  
575 southern Dora-Maira massif, Western Alps. *Schweiz. Mineral. Petrog. Mitt.*, **80**, 55-62.

576 Meffan-Main, S., Cliff, R.A., Barnicoat, A.C., Lombardo, B., Compagnoni, R. (2004): A tertiary age for  
577 Alpine high pressure metamorphism in the Gran Paradiso massif, Western Alps: a Rb-Sr  
578 microsampling study. *J. Metamorph. Geol.*, **22**, 267-281.

579 Meyer, M., Klemd, R., Hegner, E., Konopelko, D. (2014): Subduction and exhumation mechanisms of  
580 ultra-high and high-P oceanic and continental crust at Makbal (Tianshan, Kazakhstan and  
581 Kyrgyzstan). *J. Metamorph. Geol.*, **32**, 861-884.

582 Miyazaki, K., Zulkarnain, I., Sopaheluwakan, J., Wakita, K. (1996): Pressure-temperature conditions  
583 and retrograde paths of eclogites, garnet-glaucophane rocks and schists from South Sulawesi,  
584 Indonesia. *J. Metamorph. Geol.*, **14**, 549-563.

585 Moine, B., Sauvan, P., Jarousse, J. (1981): Geochemistry of evaporitic-bearing series: a tentative guide  
586 for the identification of metaevaporites. *Contrib. Miner. Petrol.*, **76**, 401-412.

587 Newton, R.C., Charlu, T.V., Kleppa, O.J. (1980): Thermochemistry of the high structural state  
588 plagioclases. *Geoch. Cosmoch. Acta*, **44**, 933-941.

589 Okay, A.I. (2002): Jadeite-chloritoid-glaucophane-lawsonite blueschists from north-west Turkey:  
590 unusually high P/T ratios in continental crust. *J. Metamorph. Geol.*, **20**, 757-768.

591 Orozbaev, R., Hirajima, T., Bakirov, A., Takasu, A., Maki, K., Yoshida, K., Sakiev, K., Bakirov, A., Hirata,  
592 T., Tagiri, M., Togonbaeva, A. (2015): Trace element characteristics of clinozoisite pseudomorphs  
593 after lawsonite in talc-garnet-chloritoid schists from the Makbal UHP Complex, northern Kyrgyz  
594 Tian-Shan. *Lithos*, **226**, 98-115.

595 Pouchou, J.L. & Pichoir, F. (1988): Determination of mass absorption coefficients for soft X-Rays by  
596 use of the electron microprobe. *Microbeam Analysis*, San Francisco Press, pp 319-324.

597 Proyer, A. (2003): Metamorphism of pelites in NKFMAH - a new petrogenetic grid with implications  
598 for the preservation of high pressure mineral assemblages during exhumation. *J. Metamorph.*  
599 *Geol.*, **21**, 493-509.

600 Pyle, J.M. & Spear, F.S. (2000): An empirical garnet (YAG)  $\pm$  xenotime thermometer. *Contrib. Mineral.*  
601 *Petrol.*, **138**, 51-58.

602 Reinecke, T. (1991): Very-high pressure metamorphism and uplift of coesite-bearing metasediments  
603 from the Zermatt-Saas zone, Western Alps. *Eur. J. Mineral.*, **3**, 7-17.

604 Schreyer, W. (1977): Whiteschists: their compositions and pressure-temperature regimes based on  
605 experimental, field and petrographic evidence. *Tectonophysics*, **34**, 127-144.



606 Selverstone, J., Morteani, G., Staude, J.M. (1991): Fluid channelling during ductile shearing:  
607 transformation of granodiorite into aluminous schist in the Tauren Window, Eastern Alps. *J.*  
608 *Metamorph. Geol.*, **9**, 419–431.

609 Smye, A.J., Greenwood, L.V., Holland, T.J.B. (2010): Garnet–chloritoid–kyanite assemblages: eclogite  
610 facies indicators of subduction constraints in orogenic belts. *J. Metamorph. Geol.*, **28**, 753–768.

611 Theye, T. & Seidel, E. (1991): Petrology of low-grade high pressure metapelites from the External  
612 Hellenides (Crete, Peloponnese). A case study with attention to sodic minerals. *Eur. J. Mineral.*, **3**,  
613 343–366.

614 Vidal, O. & Theye, T. (1996): Petrology of Fe-Mg-carpholite-bearing metasediments from NE Oman. *J.*  
615 *Metamorph. Geol.*, **14**, 381–397.

616 Warren, C.J. & Waters, D.J. (2006): Oxidized eclogites and garnet-blueschists from Oman: P–T path  
617 modelling in the NCFMASHO system. *J. Metamorph. Geol.*, **24**, 783–802.

618 Wei, C., Wang, W., Clarke, G.L., Zhang, L., Song, S. (2009): Metamorphism of high/ultrahigh-pressure  
619 pelitic-felsic schist in the South Tianshan Orogen, NW China: phase equilibria and P–T path. *J.*  
620 *Petrol.*, **50**, 1973–1991.

621 Wei, C.J. & Powell, R. (2004): Calculated phase relations in high-pressure metapelites in the system  
622 NCFMASH (Na<sub>2</sub>O–K<sub>2</sub>O–FeO–MgO–Al<sub>2</sub>O<sub>3</sub>–SiO<sub>2</sub>–H<sub>2</sub>O) with application to natural rocks. *J. Petrol.*, **44**,  
623 183–202.

624 Wei, C.J. & Powell, R. (2006): Calculated phase relations in the system NCKFMASH (Na<sub>2</sub>O–CaO–K<sub>2</sub>O–  
625 FeO–MgO–Al<sub>2</sub>O<sub>3</sub>–SiO<sub>2</sub>–H<sub>2</sub>O) for high-pressure metapelites. *J. Petrol.*, **47**, 385–408.

626 Wei, C.J. & Song, S.G. (2008): Chloritoid–glaucophane schist in the north Qilian orogen, NW China:  
627 phase equilibria and P–T path from garnet zonation. *J. Metamorph. Geol.*, **26**, 301–316.

628 White, R., Pomroy, N., Powell, R. (2005): An in-situ metatexite–diatexite transition in upper  
629 amphibolite facies rocks from Broken Hill, Australia. *J. Metamorph. Geol.*, **23**, 579–602.

630 Whitney, D.L. & Evans, B.W. (2010): Abbreviations for names of rock-forming minerals. *Am. Mineral.*,  
631 **95**, 185–187.

632

633 **Figure captions**

634

635 **Fig. 1 – (a)** Tectonic sketch map of the southern Dora-Maira Massif, with the location of Costigliole  
636 Saluzzo (modified from Castelli *et al.*, 2014). **(b)** The roman villa at Costigliole Saluzzo (from Elia *et al.*,  
637 2013; in red: room H2, where the majority of the querns come from). **(c)** A quern stone during its  
638 excavation.

639

640 **Fig. 2 – (a, b)** Rotary querns from Costigliole Saluzzo (a: specimen from US900; b: specimen from  
641 US773). **(c)** Reconstruction of a quern (from Donner & Marzoli, 1994) **(d, e, f)** Details of specimens  
642 from US773 (d), US900 (e) and US557 (f).

643

644 **Fig. 3 –** Processed major elements  $\mu$ -XRF maps of the whole thin sections of samples US900 and  
645 US773.

646

647 **Fig. 4 – (a, b)** Representative microstructures of samples US900 (a) and US773 (b) (Plane Polarized  
648 Light: PPL). **(c, d)** Garnet porphyroblasts with coesite (partially inverted to quartz) inclusion in the rim  
649 and chloritoid inclusion in the core (c: US900; d: US773) (PPL). **(e)** Zoned glaucophane nematoblasts  
650 associated to blue-green chloritoid (US900) (PPL). **(f)** Slightly zoned blue-green chloritoid partially  
651 replaced by greenish Mg-chlorite (US773) (PPL). Mineral abbreviations after Whitney & Evans (2010).

652

653 **Fig. 5 – (a-c)** Glaucophane composition plotted in the Si vs.  $Mg/(Mg+Fe^{+2})$  (a), Si vs.  $Fe^{+3}/Fe_{tot}$ , and Si  
654 vs.  $Na/(Na+Ca)$  diagrams (data from both samples US900 and US773). **(d)** Chloritoid composition  
655 plotted in the  $(Fe^{+2}+Mg)-(Al^{VI}+Fe^{+3})-Mg$  diagram (data from both samples US900 and US773).

656

657 **Fig. 6 – (a)** Garnet composition plotted in the Prp-Alm-(Sps+Grs) diagram (data from both samples  
658 US900 and US773). **(b)** Major and trace element chemical profile of a garnet porphyroblast from  
659 sample US900. Note the bell shaped profile of  $X_{Mn}$ , suggesting a prograde growth and the similar  
660 pattern of Y, Na and Cr.

661

662 **Fig. 7 – (a)** Microphotograph of large and relatively well preserved coesite inclusion within garnet  
663 mantle, and smaller polycrystalline quartz inclusions within garnet rim (US773; crossed polarized  
664 light). **(b)** Microphotograph of relatively small coesite inclusion, partly inverted to palisade quartz,  
665 within garnet rim (US773) (PPL). **(c)** Raman spectrum of coesite (US773). **(d)** Microphotograph of the  
666 mapped, well preserved coesite inclusion in garnet. The rectangle shows the mapped area reported  
667 in Fig. 7e (US773) (PPL). **(d)** Raman map of the spatial distribution and the intensity of the main peaks  
668 of coesite ( $524\text{ cm}^{-1}$ , in green), quartz ( $470\text{ cm}^{-1}$ , in blue), and garnet ( $917\text{ cm}^{-1}$ , in red). From the map  
669 is evident that the coesite inversion to quartz start from the grain-boundaries and the fractures.

670

671 **Fig. 8 – (a)** P-T pseudosection calculated for sample US900 in the MnNCFMASH system using the  
672 whole rock bulk composition (Table 3). The variance of the fields varies from three (i.e. 7 phases,  
673 light grey fields) to six (i.e. 4 phases, darker grey fields). Pink continuous, dashed and dotted lines are  
674 the  $X_{Mg}$ ,  $X_{Ca}$  and  $X_{Mn}$  isopleths of garnet corresponding to the measured composition of garnet core;  
675 light blue continuous line is the  $X_{Mg}$  isopleth of chloritoid corresponding to the measured  
676 composition of chloritoid core. P-T conditions constrained for the growth of garnet core are  
677 represented by the white dotted polygon. **(b)** P-T pseudosection calculated for sample US900 using

678 the fractionated bulk composition (whole rock composition minus garnet core and mantle; Table 3).  
679 The variance of the fields varies from three (i.e. 7 phases, light grey fields) to six (i.e. 4 phases, darker  
680 grey fields). Pink continuous, and dashed lines are the  $X_{Mg}$  and  $X_{Ca}$  isopleths of garnet corresponding  
681 to the measured composition of garnet rim; light blue continuous line is the  $X_{Mg}$  isopleth of chloritoid  
682 corresponding to the measured composition of chloritoid rim. P-T conditions constrained for the  
683 growth of garnet rim are represented by the white dotted polygon. **(c-I)** Modal variations (vol%) of  
684 the main mineral phases in sample US900 (c-i) and isomodes of water (mol) (I) calculated for the P-T  
685 pseudosection of Fig. 8b. Colours from blue to red imply higher modal proportions as indicated in  
686 each legend. The black arrow is the prograde P-T path constrained basing on the pseudosection  
687 results and YAG thermometry.

688

689 **Fig. 9** – Prograde P-T path (black arrow) inferred for the studied samples basing on the  
690 pseudosection results and YAG thermometry and comparison with the P-T evolution constrained for  
691 the adjacent UHP Brossasco-Isasca Unit (dashed grey arrow). The blue and light blue polygons  
692 represent the P-T conditions constrained for the growth of garnet core and rim, respectively (see Fig.  
693 8a, b).

694

695

696

Figure 1

[Click here to download Figure: Fig1.tif](#)

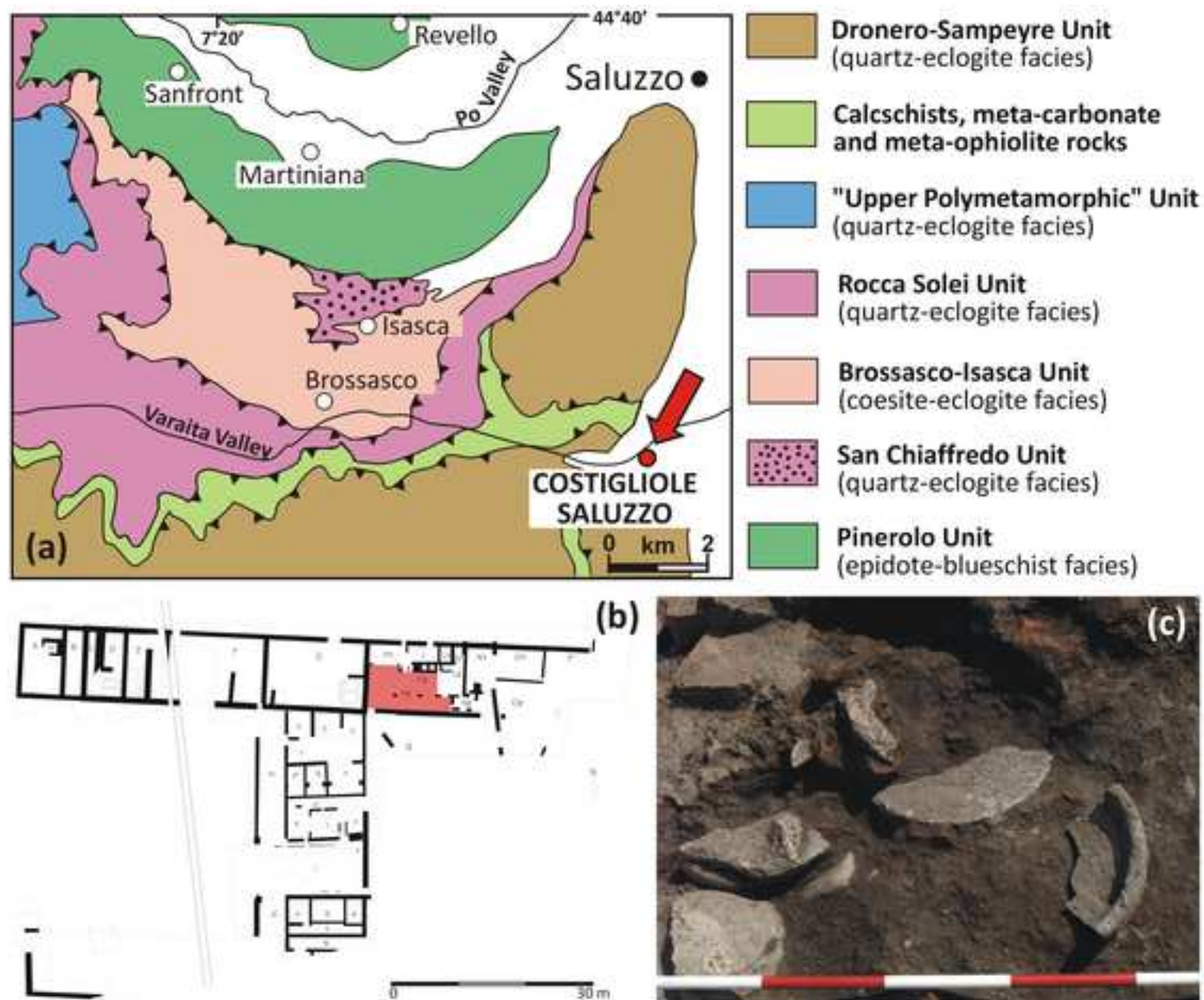


**Fig. 1.** (a) Tectonic sketch map of the southern Dora-Maira Massif, with the location of Costigliole Saluzzo (modified from Castelli et al., 2014). (b) The Roman villa at Costigliole Saluzzo (from Eila et al., 2013; in red; room HQ, where the majority of the querns come from). (c) A quern stone during its excavation.



Figure 2

[Click here to download Figure: Fig2.tif](#)

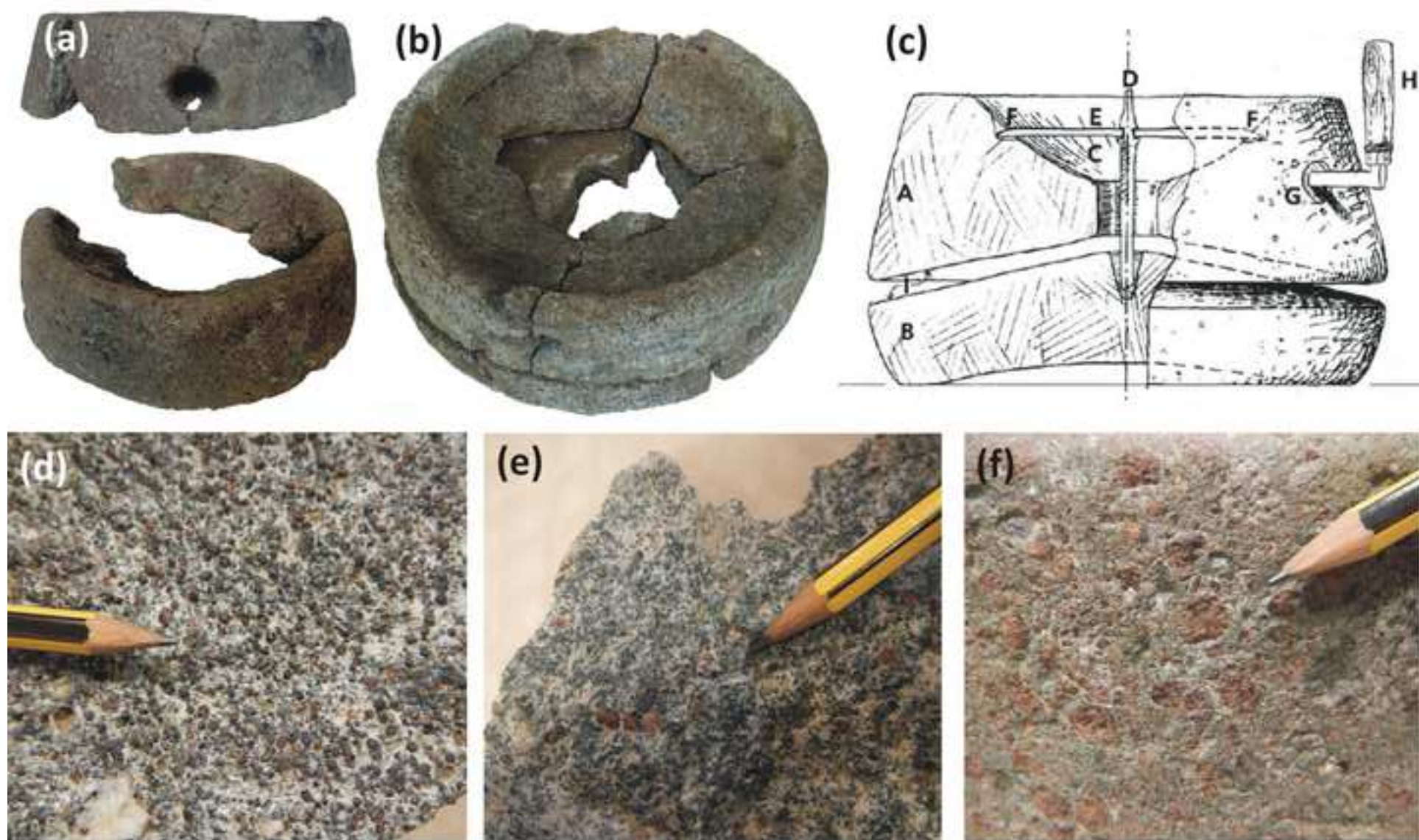


**Fig. 2** (a, b) Rotary querns from Costigliole Saluzzo (a: specimen from US900; b: specimen from US773). (c) Reconstruction of a quern (from Donner & Marzoli, 1994) (d, e, f) Details of specimens from US773 (d), US900 (e) and US557 (f).



Figure 3

[Click here to download Figure: Fig3.tif](#)

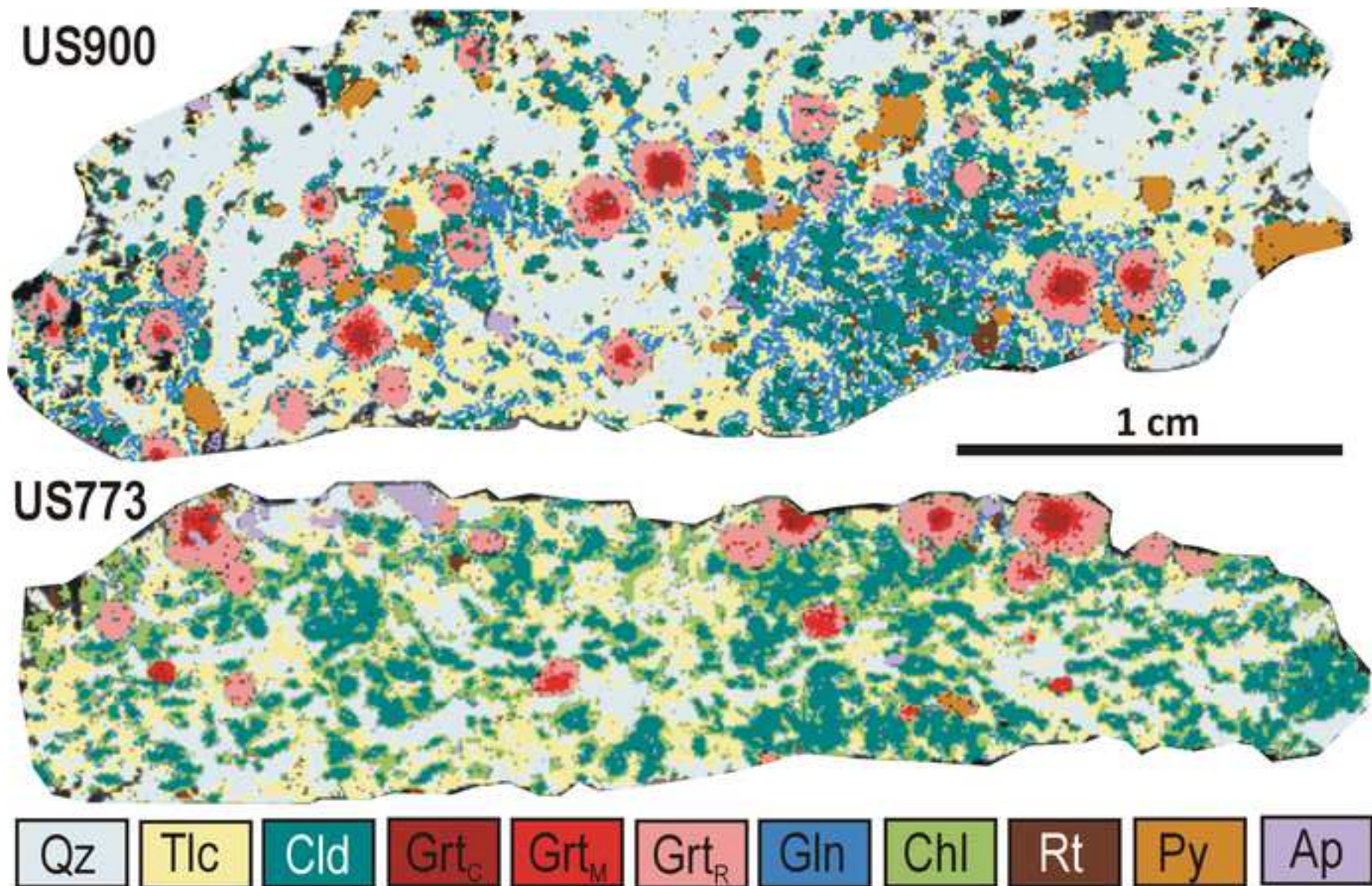
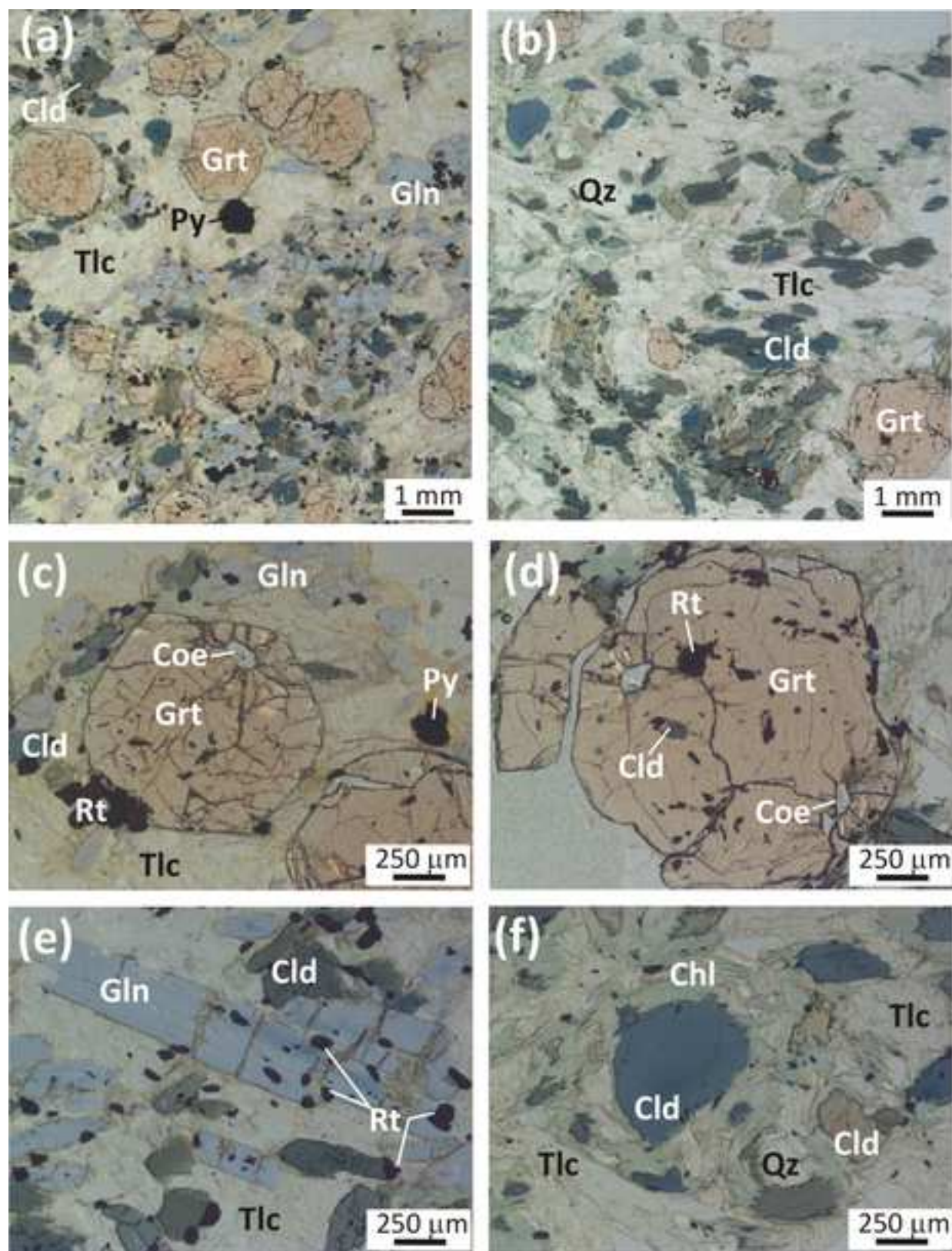


**Fig. 3** Processed major elements  $\mu$ -XRF maps of the whole thin sections of samples US900 and Us773.



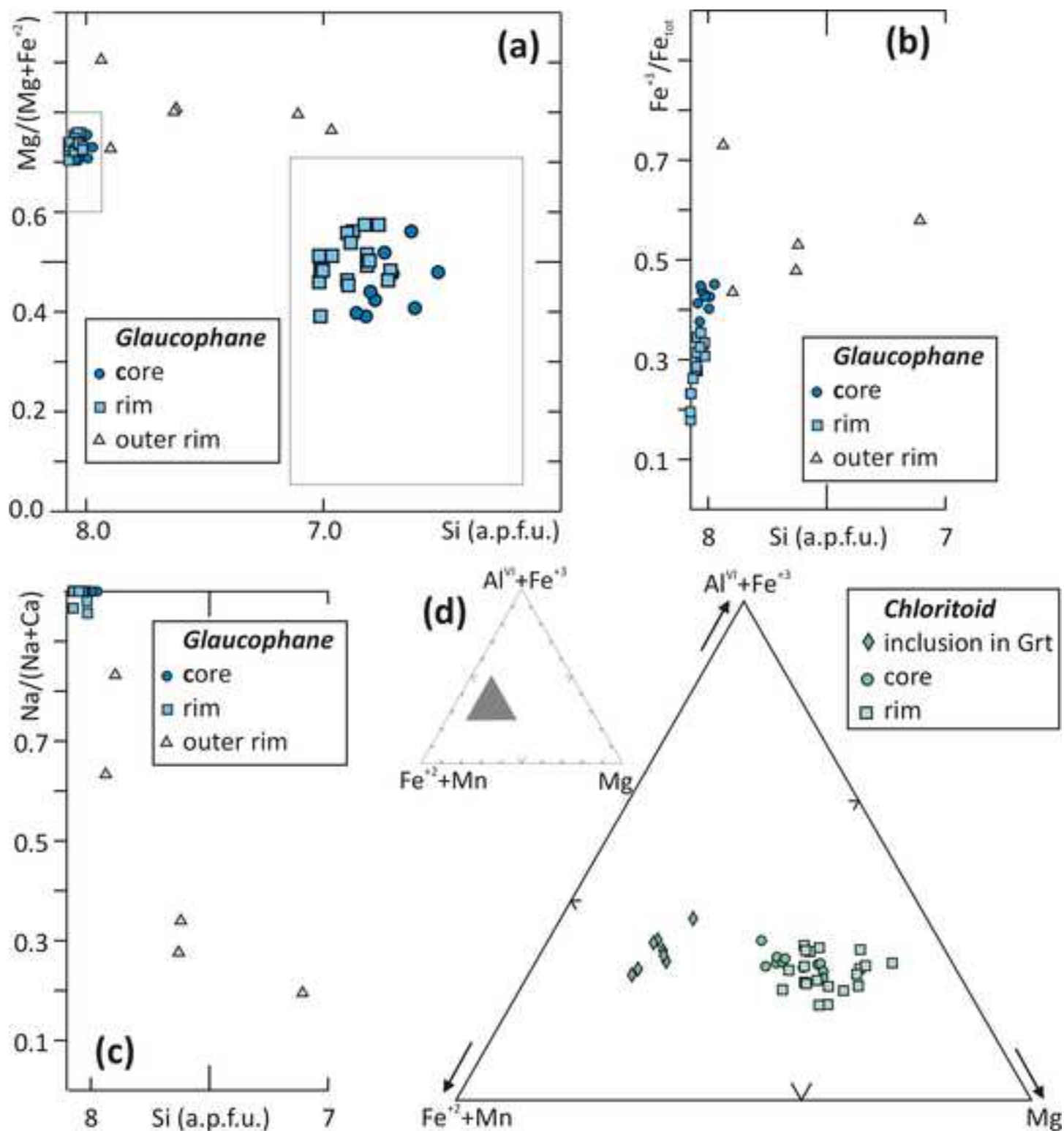
Figure 4

[Click here to download Figure: Fig4.tif](#)



**Fig. 4** (a, b) Representative microstructures of samples US900 (a) and US773 (b) (Plane Polarized Light: PPL). (c, d) Garnet porphyroblasts with coesite [partially inverted to quartz] inclusion in the rim and chloritoid inclusion in the core (c: US900; d: US773) (PPL). (e) Zoned glaucophane nematoblasts associated to blue-green chloritoid (US900) (PPL). (f) Slightly zoned blue-green chloritoid partially replaced by greenish Mg-chlorite (US773) (PPL). Mineral abbreviations after Whitney & Evans (2010).

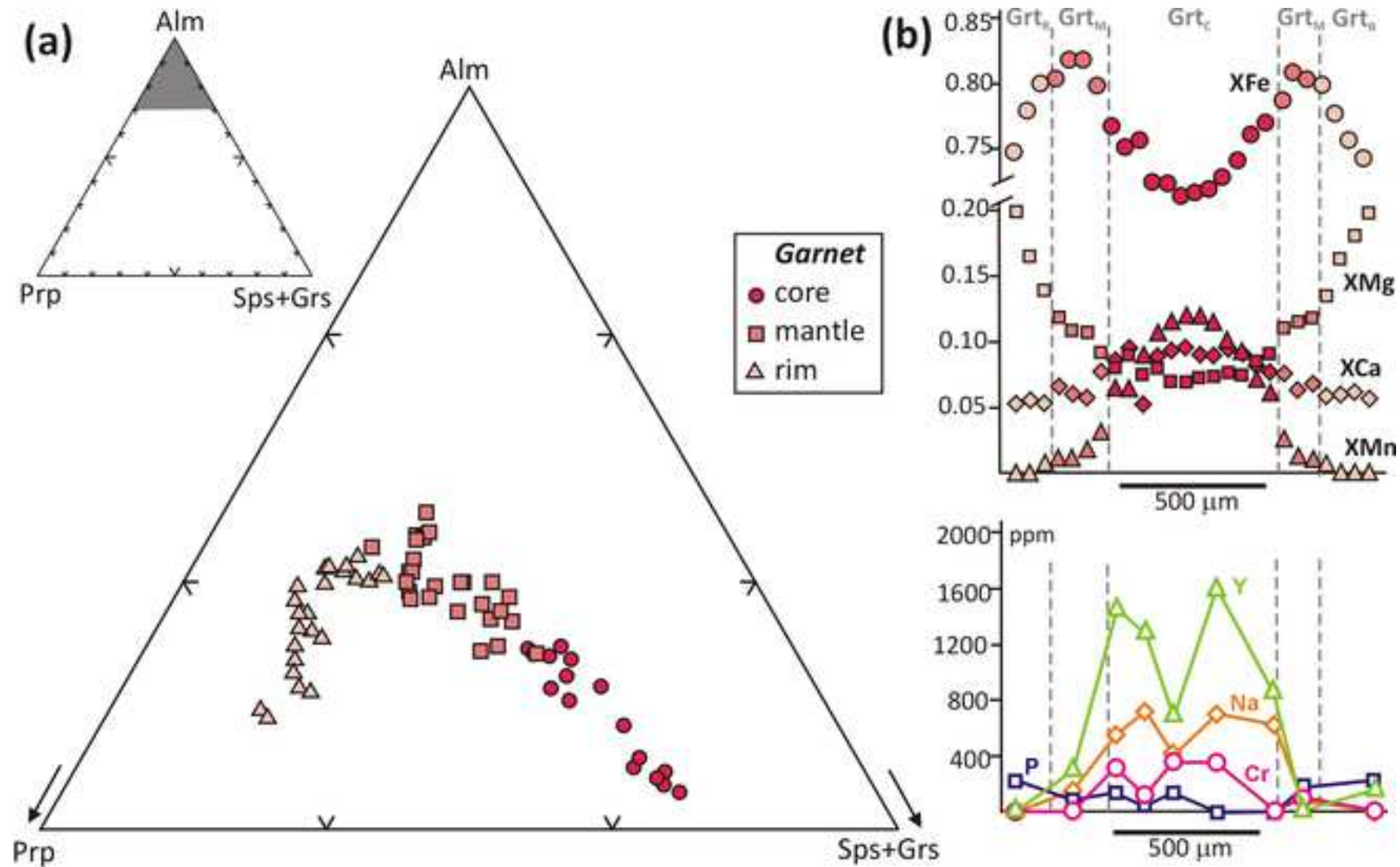
Figure 5  
[Click here to download Figure: Fig5.tif](#)



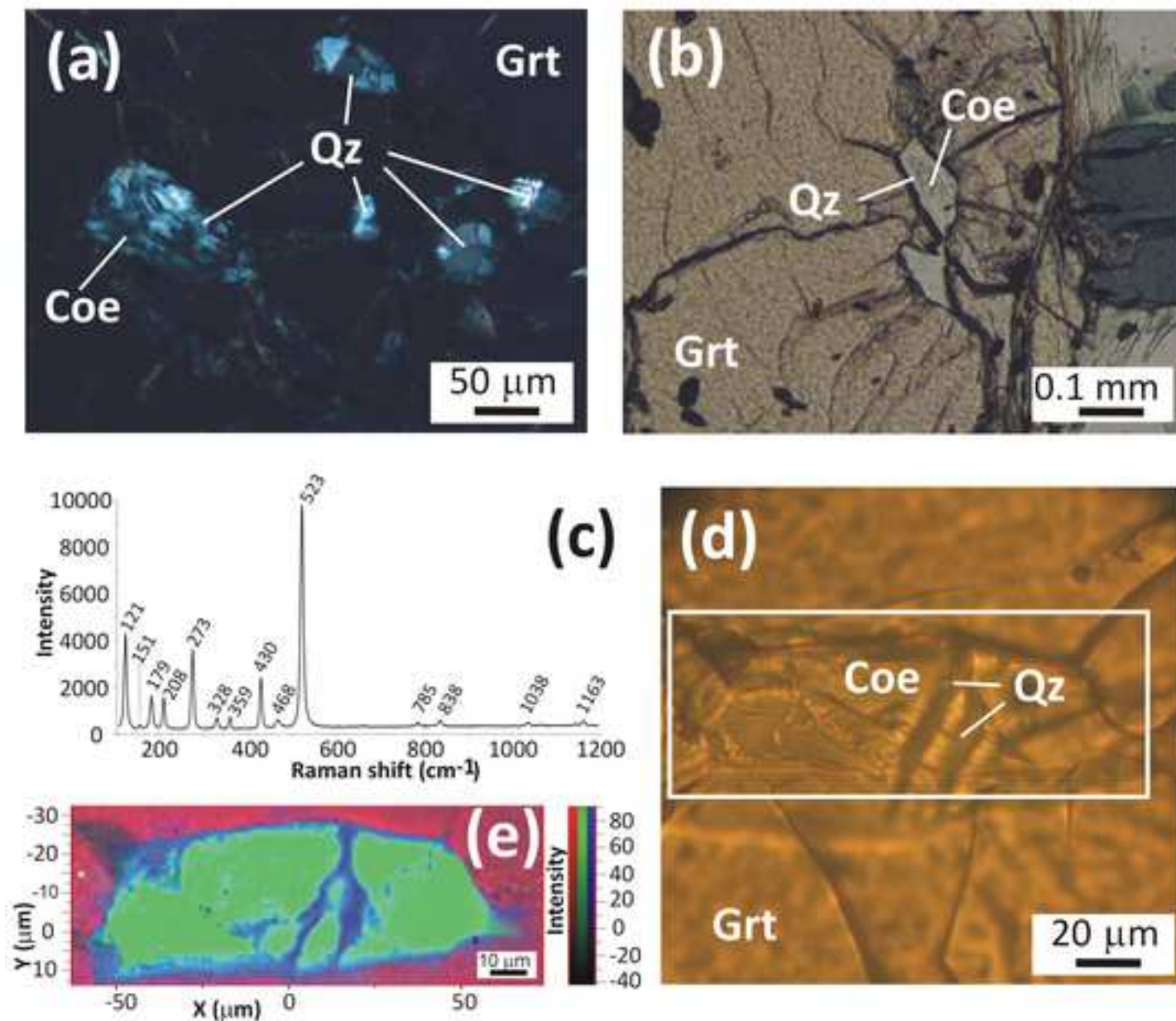
**Fig. 5 (a-c)** Glaucophane composition plotted in the Si vs. Mg/(Mg+Fe<sup>3+</sup>) (a), Si vs. Fe<sup>3+</sup>/Fe<sub>tot</sub>, and Si vs. Na/(Na+Ca) diagrams (data from both samples US900 and US773). **(d)** Chloritoid composition plotted in the (Fe<sup>2+</sup>+Mg)-(Al<sup>VI</sup>+Fe<sup>3+</sup>)-Mg diagram (data from both samples US900 and US773).



Figure 6  
[Click here to download Figure: Fig6.tif](#)



**Fig. 6** (a) Garnet composition plotted in the Prp-Alm-(Sps+Grs) diagram (data from both samples US900 and US773). (b) Major and trace element chemical profile of a garnet porphyroblast from sample US900. Note the bell shaped profile of  $X_{\text{Fe}}$ , suggesting a prograde growth and the similar pattern of Y, Na and Cr.



**Fig. 7** (a) Microphotograph of large and relatively well preserved coesite inclusion within garnet mantle, and smaller polycrystalline quartz inclusions within garnet rim (US773; crossed polarized light). (b) Microphotograph of relatively small coesite inclusion, partly inverted to palisade quartz, within garnet rim (US773) (PPL). (c) Raman spectrum of coesite (US773). (d) Microphotograph of the mapped, well preserved coesite inclusion in garnet. The rectangle shows the mapped area reported in Fig. 7e (US773) (PPL). (e) Raman map of the spatial distribution and the intensity of the main peaks of coesite (524  $\text{cm}^{-1}$ , in green), quartz (470  $\text{cm}^{-1}$ , in blue), and garnet (917  $\text{cm}^{-1}$ , in red). From the map is evident that the coesite inversion to quartz start from the grain-boundaries and the fractures.



Figure 8  
 Click here to download Figure: Fig8.tif

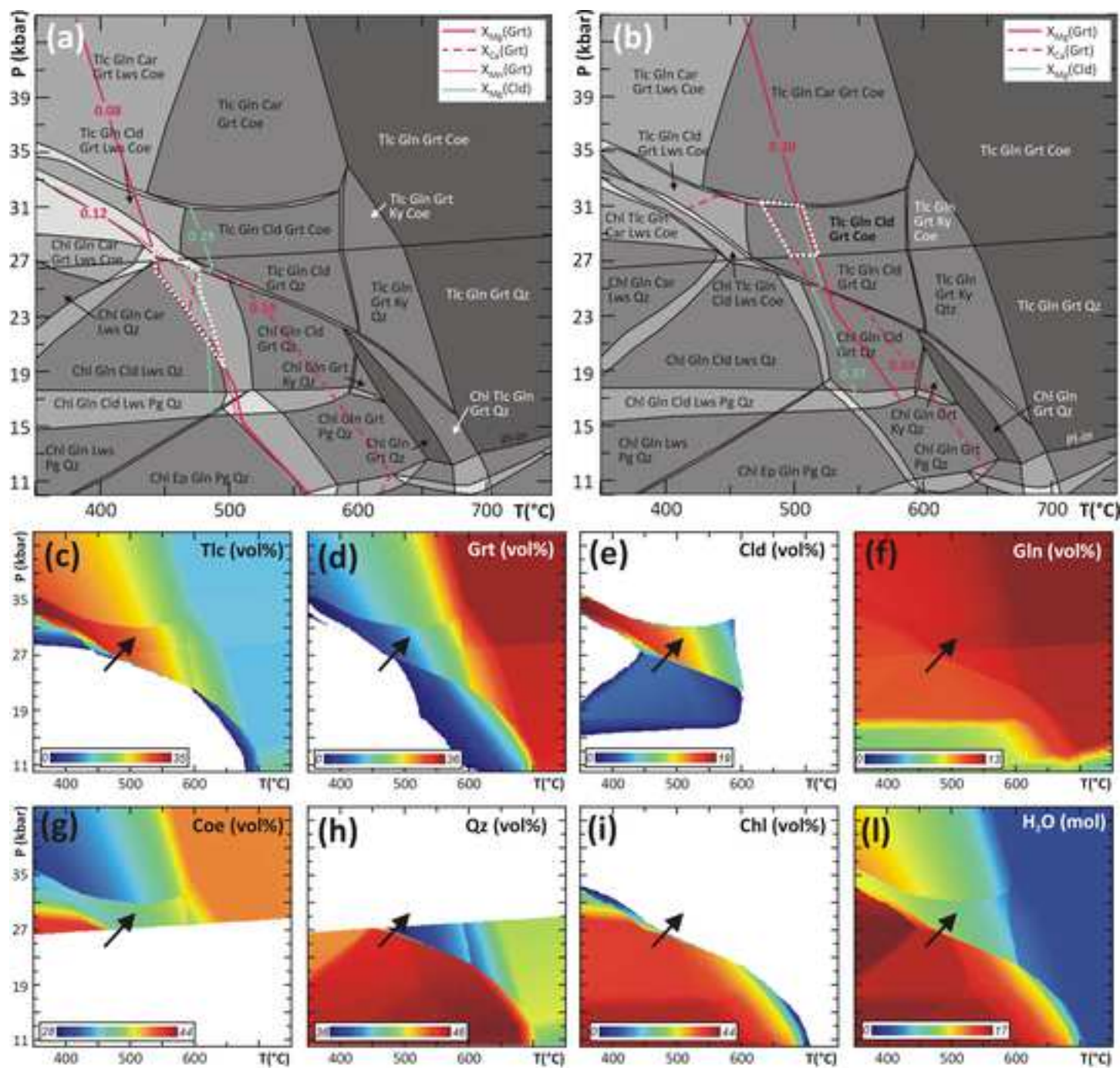


**Fig. 8** (a) P-T pseudosection calculated for sample US900 in the MnNCFMASH system using the whole rock bulk composition (Table 3). The variance of the fields varies from three (i.e. 7 phases, light grey fields) to six (i.e. 4 phases, darker grey fields). Pink continuous, dashed and dotted lines are the  $X_{Mg}$ ,  $X_{Ca}$  and  $X_{Mn}$  isopleths of garnet corresponding to the measured composition of garnet core; light blue continuous line is the  $X_{Mg}$  isopleth of chloritoid corresponding to the measured composition of chloritoid core. P-T conditions constrained for the growth of garnet core are represented by the white dotted polygon. (b) P-T pseudosection calculated for sample US900 using the fractionated bulk composition (whole rock composition minus garnet core and mantle; Table 3). The variance of the fields varies from three (i.e. 7 phases, light grey fields) to six (i.e. 4 phases, darker grey fields). Pink continuous, and dashed lines are the  $X_{Mg}$  and  $X_{Ca}$  isopleths of garnet corresponding to the measured composition of garnet rim; light blue continuous line is the  $X_{Mg}$  isopleth of chloritoid corresponding to the measured composition of chloritoid rim. P-T conditions constrained for the growth of garnet rim are represented by the white dotted polygon. (c-l) Modal variations (vol%) of the main mineral phases in sample US900 (c-i) and isomodes of water (mol) (l) calculated for the P-T pseudosection of Fig. 8b. Colours from blue to red imply higher modal proportions as indicated in each legend. The black arrow is the prograde P-T path constrained basing on the pseudosection results and YAG thermometry.

Figure 9

[Click here to download Figure: Fig9.tif](#)

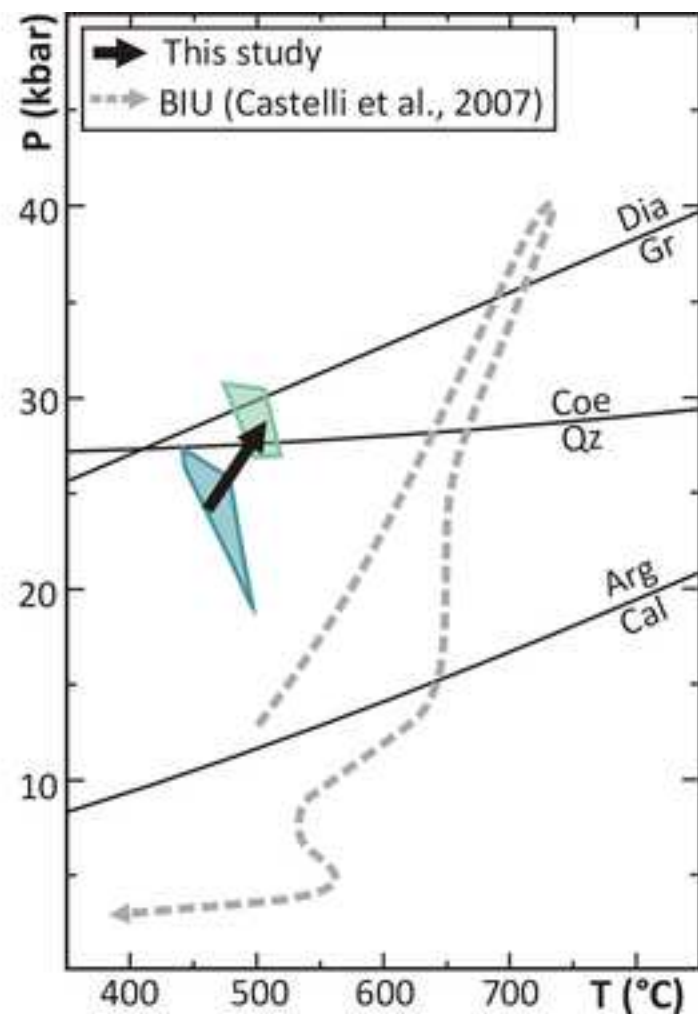


**Fig. 9** Prograde P-T path (black arrow) inferred for the studied samples basing on the pseudosection results and YAG thermometry and comparison with the P-T evolution constrained for the adjacent UHP Brossasco-Isasca Unit (dashed grey arrow). The blue and light blue polygons represent the P-T conditions constrained for the growth of garnet core and rim, respectively (see Fig. 8a, b).

Table 1. Representative WDS a

Sample Analysis	US900									773_1 rim
	900_23 rim	900_24 mantle	900_25	900_26	900_27 core			900_28	900_29	
SiO <sub>2</sub>	37.52	36.86	37.40	37.01	36.60	36.88	37.14	36.89	37.32	37.67
P <sub>2</sub> O <sub>5</sub>	0.05	0.02	0.03	0.01	0.03	0.00	0.00	0.04	0.05	0.01
TiO <sub>2</sub>	0.00	0.04	0.00	0.08	0.10	0.07	0.02	0.08	0.02	0.05
Al <sub>2</sub> O <sub>3</sub>	21.16	20.61	20.88	20.62	20.56	20.67	20.70	20.77	21.50	21.12
Cr <sub>2</sub> O <sub>3</sub>	0.00	0.00	0.05	0.02	0.05	0.05	0.00	0.01	0.00	0.00
Y <sub>2</sub> O <sub>3</sub>	0.00	0.04	0.18	0.16	0.08	0.20	0.11	0.00	0.02	0.00
FeO	34.93	37.01	35.15	33.06	32.19	33.34	34.55	36.73	34.33	35.23
MnO	0.16	0.54	1.80	4.01	4.77	4.34	2.80	0.47	0.16	0.18
MgO	4.40	2.77	2.34	1.96	1.79	1.93	2.18	2.89	4.72	4.48
NiO	0.00	0.03	0.02	0.00	0.24	0.00	0.00	0.00	0.11	0.00
CaO	1.90	2.01	2.70	2.79	3.10	2.80	2.60	2.17	2.00	1.70
Na <sub>2</sub> O	0.00	0.02	0.07	0.10	0.06	0.09	0.09	0.01	0.00	0.00
K <sub>2</sub> O	0.00	0.00	0.00	0.02	0.00	0.00	0.01	0.01	0.01	0.01
Total	100.10	99.95	100.62	99.83	99.56	100.36	100.19	100.06	100.22	100.44
Si	2.988	2.979	3.003	3.001	2.979	2.979	2.999	2.974	2.960	2.992
P	0.003	0.001	0.002	0.001	0.002	0.000	0.000	0.003	0.003	0.001
Ti	0.000	0.002	0.000	0.005	0.006	0.004	0.001	0.005	0.001	0.003
Al	1.986	1.964	1.976	1.971	1.972	1.967	1.969	1.973	2.010	1.977
Cr	0.000	0.000	0.003	0.001	0.003	0.003	0.000	0.001	0.000	0.000
Y	0.000	0.002	0.008	0.007	0.004	0.009	0.005	0.000	0.001	0.000
Fe <sup>+3</sup>	0.033	0.073	0.015	0.025	0.056	0.069	0.041	0.069	0.063	0.034
Fe <sup>+2</sup>	2.293	2.429	2.345	2.217	2.135	2.183	2.292	2.407	2.214	2.306
Mn	0.010	0.037	0.123	0.275	0.329	0.297	0.192	0.032	0.011	0.012
Mg	0.522	0.334	0.281	0.237	0.217	0.233	0.262	0.348	0.558	0.531
Ni	0.000	0.002	0.001	0.000	0.016	0.000	0.000	0.000	0.007	0.000
Ca	0.162	0.174	0.232	0.242	0.270	0.243	0.225	0.187	0.170	0.144
Na	0.000	0.003	0.011	0.015	0.009	0.014	0.014	0.002	0.000	0.000
K	0.000	0.000	0.000	0.002	0.000	0.000	0.001	0.001	0.001	0.001
XMg	0.18	0.11	0.09	0.08	0.08	0.08	0.09	0.12	0.19	0.18
XFe	0.77	0.82	0.78	0.74	0.72	0.74	0.77	0.81	0.75	0.77
XCa	0.05	0.06	0.08	0.08	0.09	0.08	0.08	0.06	0.06	0.05
XMn	0.00	0.01	0.04	0.09	0.11	0.10	0.06	0.01	0.00	0.00

Structural formulae have been calculated on the basis of 12 oxygens. Fe<sup>+3</sup> has been calculated by stoichiometry.

analysis of garnet

US773										
m	773_2	773_3	773_4 mantle	773_5	773_6 core	773_7	773_8 mantle	773_9	773_10 rim	773_11
	36.99	36.84	36.93	37.21	36.82	36.85	36.91	37.19	37.18	37.68
	0.05	0.09	0.01	0.05	0.00	0.04	0.00	0.00	0.12	0.00
	0.07	0.07	0.11	0.05	0.07	0.05	0.17	0.06	0.01	0.15
	20.67	20.63	20.19	20.40	20.34	20.72	20.49	20.73	20.96	21.28
	0.00	0.05	0.04	0.04	0.05	0.01	0.07	0.00	0.00	0.00
	0.00	0.12	0.02	0.00	0.25	0.00	0.02	0.00	0.00	0.00
	36.50	36.96	36.80	35.86	34.39	35.78	35.86	36.47	35.91	34.84
	0.16	0.32	0.58	1.23	2.72	1.15	0.37	0.19	0.11	0.12
	3.72	2.82	2.41	2.29	2.22	2.52	2.94	3.33	4.00	4.62
	0.00	0.00	0.14	0.00	0.05	0.09	0.17	0.13	0.14	0.00
	1.50	2.54	2.87	3.01	3.12	2.89	2.62	2.08	1.48	1.84
	0.00	0.03	0.02	0.00	0.07	0.03	0.00	0.04	0.03	0.01
	0.00	0.00	0.00	0.01	0.00	0.02	0.00	0.02	0.02	0.01
	99.64	100.47	100.12	100.15	100.09	100.15	99.63	100.23	99.95	100.55
	2.981	2.959	2.986	3.004	2.979	2.970	2.986	2.983	2.977	2.984
	0.003	0.006	0.000	0.003	0.000	0.003	0.000	0.000	0.008	0.000
	0.004	0.004	0.007	0.003	0.004	0.003	0.011	0.004	0.001	0.009
	1.963	1.953	1.924	1.942	1.939	1.967	1.954	1.960	1.978	1.986
	0.000	0.003	0.003	0.003	0.003	0.001	0.004	0.000	0.000	0.000
	0.000	0.005	0.001	0.000	0.011	0.000	0.001	0.000	0.000	0.000
	0.062	0.108	0.090	0.037	0.091	0.089	0.048	0.075	0.061	0.030
	2.398	2.375	2.398	2.384	2.235	2.323	2.378	2.372	2.343	2.278
	0.011	0.022	0.040	0.084	0.186	0.078	0.025	0.013	0.007	0.008
	0.447	0.338	0.291	0.276	0.267	0.303	0.355	0.399	0.477	0.546
	0.000	0.000	0.009	0.000	0.003	0.006	0.011	0.008	0.009	0.000
	0.130	0.219	0.249	0.260	0.270	0.250	0.227	0.179	0.127	0.156
	0.000	0.005	0.003	0.000	0.011	0.005	0.000	0.006	0.005	0.002
	0.000	0.000	0.000	0.001	0.000	0.002	0.000	0.002	0.002	0.001
	0.15	0.11	0.10	0.09	0.09	0.10	0.12	0.14	0.16	0.18
	0.80	0.80	0.80	0.79	0.75	0.78	0.79	0.80	0.79	0.76
	0.04	0.07	0.08	0.09	0.09	0.08	0.08	0.06	0.04	0.05
	0.00	0.01	0.01	0.03	0.06	0.03	0.01	0.00	0.00	0.00

**Table 2. Representative SEM-EDS analysis of chloritoid, g**

Chloritoid						Amphibole			
Sample Analysis	US900		US773			Sample Analysis	US900		
	2Ctd2 core	2Ctd3 rim	1Ctd46 in Grt	2Ctd11 core	2Ctd12 rim		2Gln8 core	2Gln9 rim	1Gln60 core
SiO <sub>2</sub>	24.79	24.87	24.20	24.51	24.75	SiO <sub>2</sub>	56.30	56.22	56.25
Al <sub>2</sub> O <sub>3</sub>	38.80	38.57	37.78	37.57	37.70	Al <sub>2</sub> O <sub>3</sub>	8.24	9.46	7.60
FeO	22.97	22.17	26.81	24.70	23.35	FeO	12.38	8.91	13.09
MnO	0.00	0.00	0.00	0.00	0.00	MnO	0.00	0.00	0.00
MgO	5.47	6.25	3.54	4.84	5.89	MgO	10.27	11.04	10.32
CaO	0.00	0.00	0.00	0.00	0.00	CaO	0.00	0.00	0.00
Na <sub>2</sub> O	0.00	0.00	0.00	0.00	0.00	Na <sub>2</sub> O	6.58	6.70	6.53
K <sub>2</sub> O	0.00	0.00	0.00	0.00	0.00	K <sub>2</sub> O	0.00	0.00	0.00
Total	92.03	91.86	92.33	91.61	91.68	Total	95.87	94.42	95.89
Si	2.027	2.026	2.008	2.029	2.031	Si	8.035	8.051	8.043
Al	3.737	3.704	3.694	3.664	3.646	Al	1.386	1.597	1.281
Fe <sup>+3</sup>	0.210	0.244	0.290	0.278	0.292	Fe <sup>+3</sup>	0.555	0.299	0.646
Fe <sup>+2</sup>	1.360	1.267	1.570	1.432	1.311	Fe <sup>+2</sup>	0.922	0.768	0.920
Mn	0.000	0.000	0.000	0.000	0.000	Mn	0.000	0.000	0.00
Mg	0.666	0.759	0.438	0.597	0.720	Mg	2.185	2.357	2.200
Ca	0.000	0.000	0.000	0.000	0.000	Ca	0.000	0.000	0.000
Na	0.000	0.000	0.000	0.000	0.000	Na	1.821	1.860	1.810
K	0.000	0.000	0.000	0.000	0.000	K	0.000	0.000	0.000
XMg	0.33	0.38	0.22	0.29	0.36	XMg	0.70	0.75	0.71
XFe <sup>+3</sup>	0.05	0.06	0.07	0.07	0.07	XFe <sup>+3</sup>	0.29	0.16	0.34

Structural formulae have been calculated on the basis of 14 oxygens for chloritoid, 13CNK (Si+Al+Mg+Ti+Mn+Fe=13) for amphibole. Fe<sup>+3</sup> has been calculated by stoichiometry except for amphibole (average Fe<sup>+3</sup> values).

**laucophane, talc and Mg-chlorite**

US773		Sample Analysis	Talc		Chlorite	
1Gln62 rim	1Gln70 o-rim		US900 1Tlc27	US773 2Tlc23	US773 2Chl21	
56.97	54.71	SiO <sub>2</sub>	61.53	61.49	SiO <sub>2</sub>	27.95
9.43	4.32	Al <sub>2</sub> O <sub>3</sub>	0.00	0.00	Al <sub>2</sub> O <sub>3</sub>	20.06
9.39	10.76	FeO	6.94	6.99	FeO	17.31
0.00	0.00	MnO	0.00	0.00	MnO	0.00
11.08	15.56	MgO	26.50	26.19	MgO	22.05
0.00	3.01	CaO	0.00	0.00	CaO	0.00
6.68	2.87	Na <sub>2</sub> O	0.00	0.00	Na <sub>2</sub> O	0.00
0.00	0.00	K <sub>2</sub> O	0.00	0.00	K <sub>2</sub> O	0.00
95.67	93.30	Total	94.97	94.67	Total	87.36
8.064	7.937	Si	4.032	4.046	Si	2.825
1.573	0.739	Al	0.000	0.000	Al	2.390
0.291	0.953	Fe <sup>+3</sup>	0.000	0.000	Fe <sup>+3</sup>	0.000
0.821	0.352	Fe <sup>+2</sup>	0.380	0.385	Fe <sup>+2</sup>	1.463
0.00	0.00	Mn	0.000	0.000	Mn	0.000
2.338	3.365	Mg	2.588	2.569	Mg	3.322
0.000	0.468	Ca	0.000	0.000	Ca	0.000
1.833	0.807	Na	0.000	0.000	Na	0.000
0.000	0.000	K	0.000	0.000	K	0.000
0.74	0.91	XMg	0.87	0.87	XMg	0.69
0.16	0.56					

or amphibole, 12 oxygens for talc and 18 oxygens for chlorite.



**Table 3. Bulk compositions (wt%) and modal amounts (vol%) of the main mineral phases**

Sample	US900	US900*	US773
SiO <sub>2</sub>	66.45	67.01	51.56
Al <sub>2</sub> O <sub>3</sub>	10.49	10.3	18.52
MgO	10.67	10.84	13.37
CaO	0.21	0.17	0.19
MnO	0.08	0.01	0.06
FeO	10.13	9.65	14.92
Fe <sub>2</sub> O <sub>3</sub>	1.05	1.08	1.09
Na <sub>2</sub> O	0.93	0.95	0.29
Total	100.0	100.0	100.0
Qz/Coe	38.4		21.4
Tlc	30.5		22.3
Cld	14.0		22.6
Grt	7.9		8.1
Gln	9.2		2.8
Mg-Chl	<1		22.8

\* effective bulk composition in equilibrium during the growth of Grt rim (whole rock composition minus the garnet core and mantle compositions)

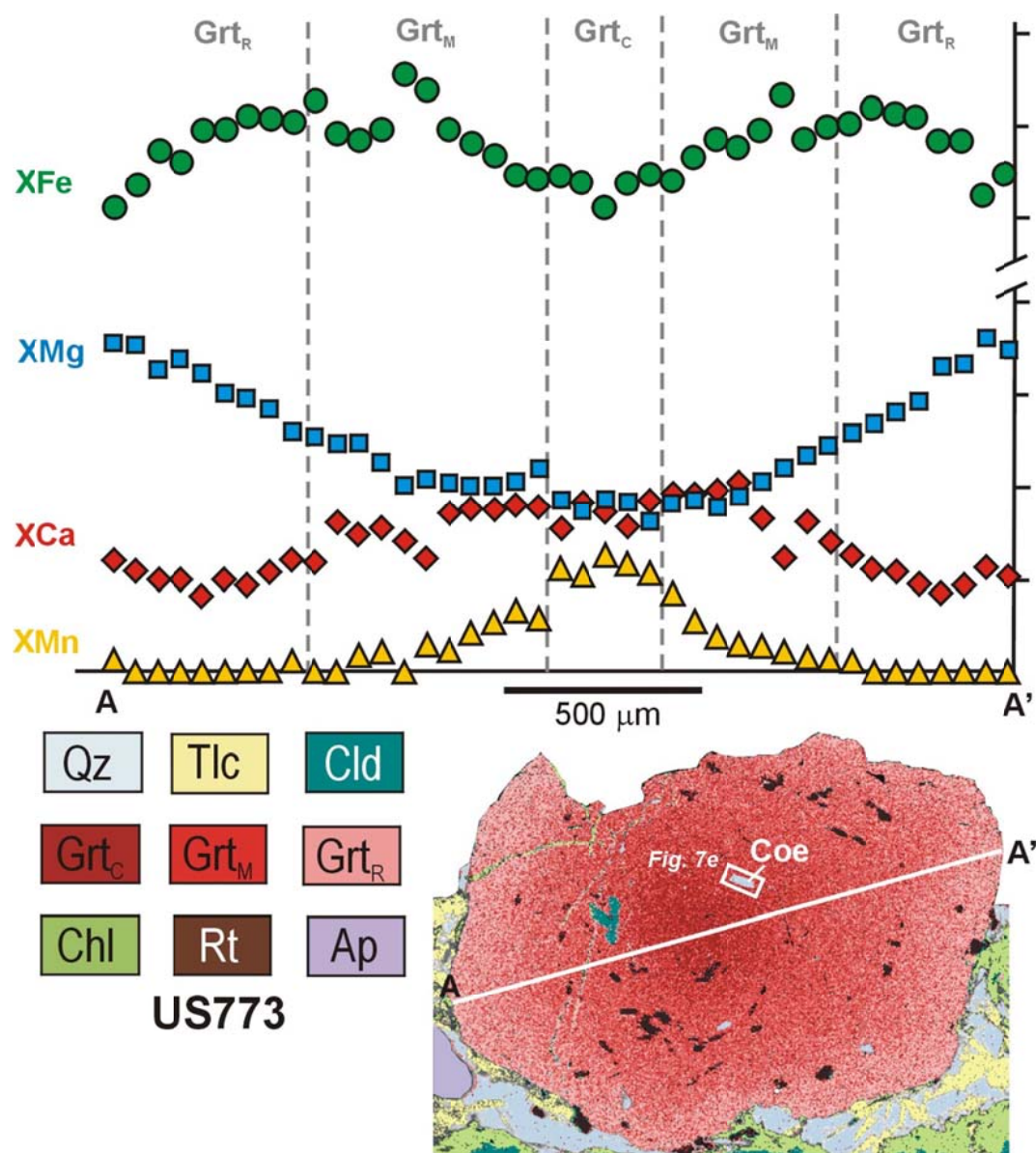


**Fig. S1** - Major element chemical profile and processed X-ray map of a garnet porphyroblast from sample US773.

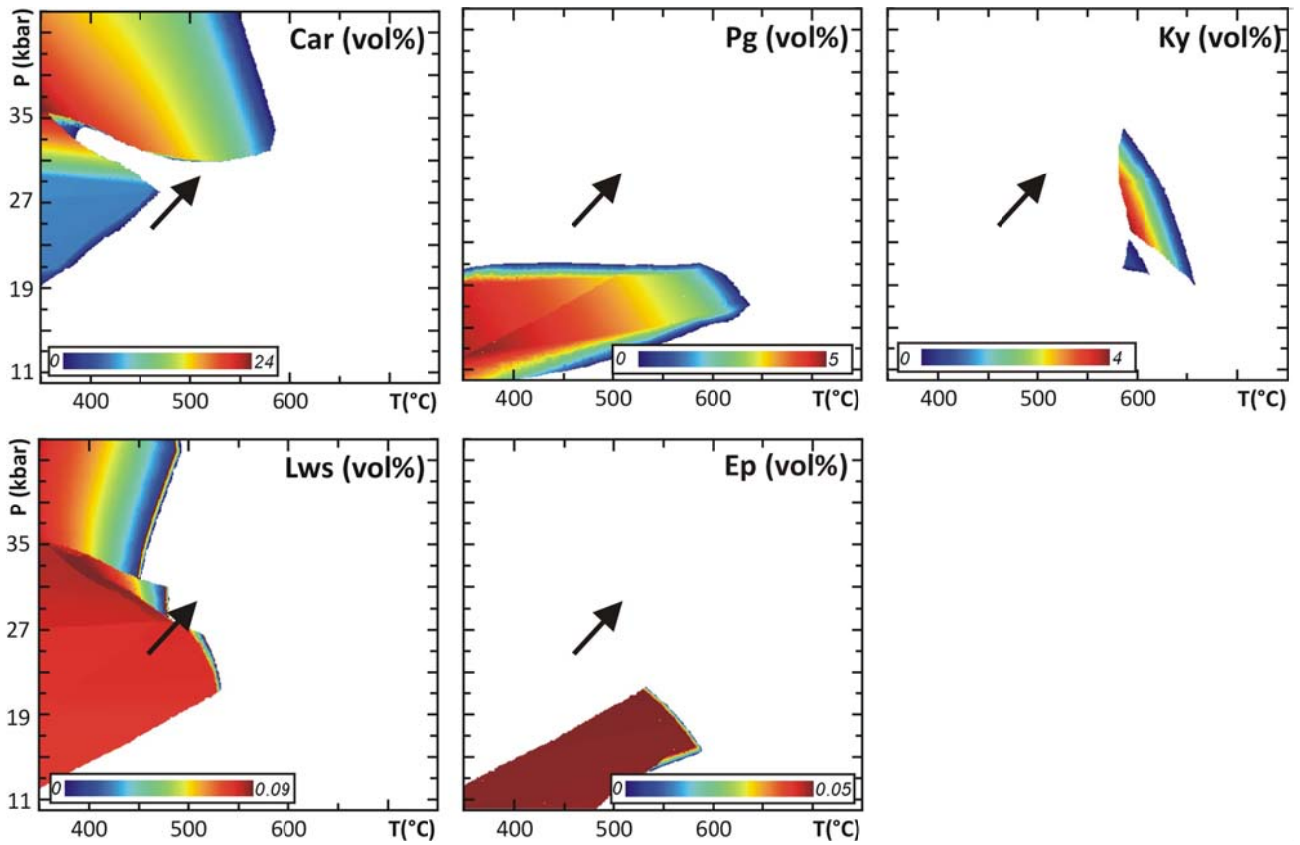


**Fig. S2** - Modal variations (vol%) of mineral phases in sample US900, not reported in Fig. 8. Colours from blue to red imply higher modal proportions as indicated in each legend. The black arrow is the prograde P-T path constrained basing on the pseudosection results and YAG thermometry.

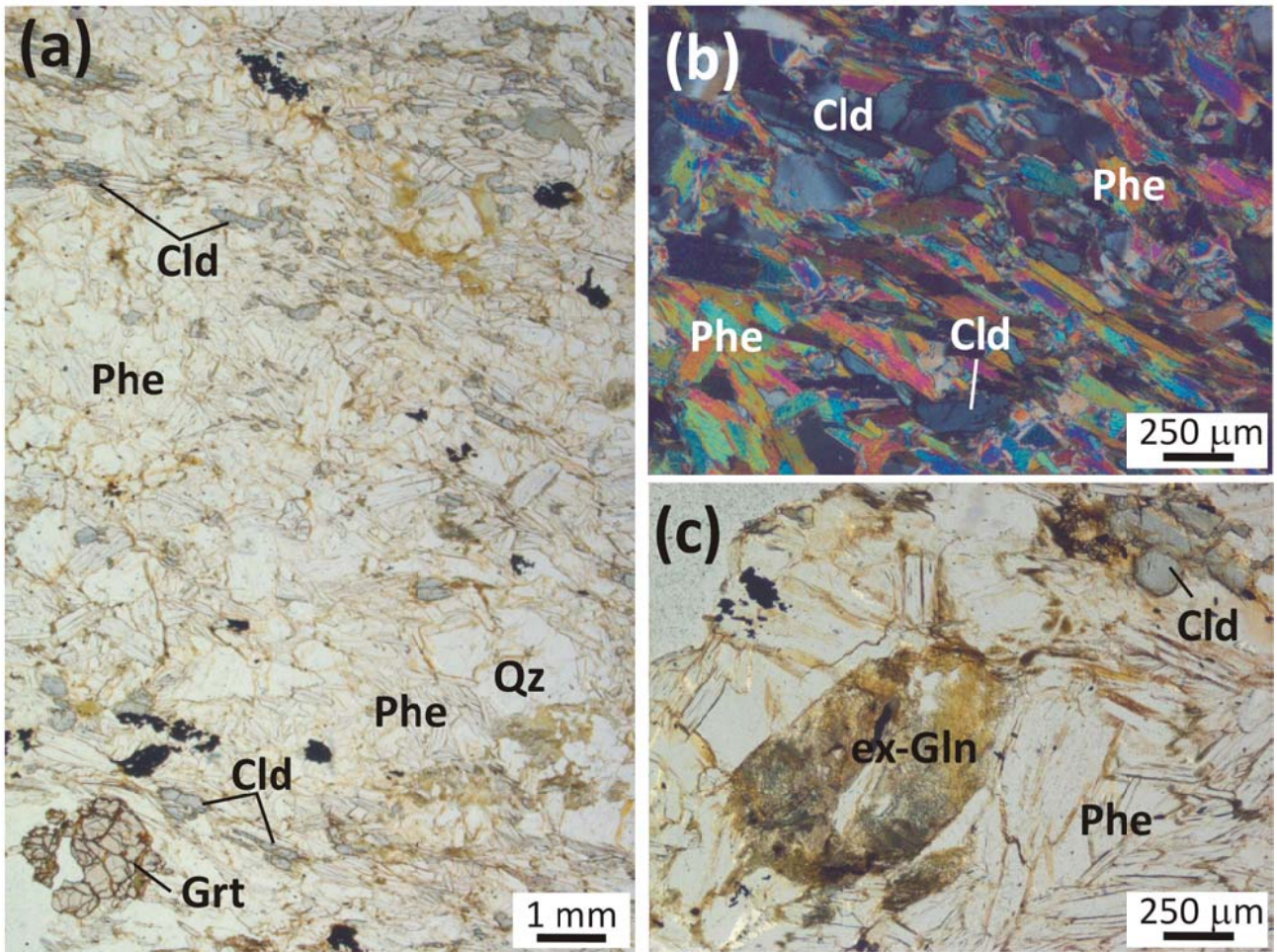


**Fig. S3** - Sample LA13. (a) Representative microstructure of sample LA13 (PPL). (b) Detail of the main foliation defined by Phe and Cld (XPL). (c) Wm + Bt + Chl pseudomorph after former Gln (PPL).